3D Image Reconstruction of Retina using Aplanats

Loke Sankrandan

A Thesis Submitted to

Indian Institute of Technology Hyderabad

In Partial Fulfillment of the Requirements for

The Degree of Master of Technology

भारतीय प्रौद्योगिकी संस्थान हैदराबाद
Indian Institute of Technology Hyderabad

Department of Electrical Engineering

June 2018

Declaration

I declare that this written submission represents my ideas in my own words, and where others' ideas or words have been included, I have adequately cited and referenced the original sources. I also declare that I have adhered to all principles of academic honesty and integrity and have not misrepresented or fabricated or falsified any idea/data/fact/source in my submission. I understand that any violation of the above will be a cause for disciplinary action by the Institute and can also evoke penal action from the sources that have thus not been properly cited, or from whom proper permission has not been taken when needed.
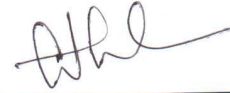
L. Sankrandan

(Signature)
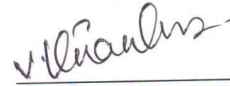
LOKE SANKRANDAN

(– Student Name –)

EE13B17M000001

(Roll No)

Approval Sheet

This thesis entitled "3D Image Reconstruction of Retina using Aplanats" by Loke Sankrandan is approved for the degree of Master of Technology from IIT Hyderabad.

(Dr. Sumohana Channappayya) Examiner
Department of Electrical Engineering
Indian Institute of Technology Hyderabad

(Dr. Kiran Kumar Vupparaboina) Examiner
Srujana Innovation Center
L. V. Prasad Eye Institute Hyderabad

(Dr. Soumya Jana) Adviser
Department of Electrical Engineering
Indian Institute of Technology Hyderabad

(Dr. Sumohana Channappayya) Chairman
Department of Electrical Engineering
Indian Institute of Technology Hyderabad

Acknowledgements

Dedication

I dedicate this humble work to my parents and to my guide. They have had tremendous influence in shaping my life to a good form.

Abstract

Existing fundus cameras provide two-dimensional images for the fundus or retina which are curved in shape, thereby distorting the peripheral information. For a quality and aberration free image, a system of lenses need to be incorporated for imaging. But that comes with narrow field of view, high-cost, and makes it bulkier and difficult to operate. Retinal abnormalities outside the photographic field cannot be captured with narrow field of view. Any compromise with the quality of imaging system will lead to poor fundus image quality. In this thesis, an attempt has been made to demonstrate that aplanats can be used to replace the lens system in fundus cameras with the benefit of acheiving high field of views of about 200° without any pupil dialation needed. Aplanats are aberration free and have high numerical apertures. Therefore, they can even collect highly diverging rays. But due to their design, complete retina cannot be imaged using a single aplanat. So a three phase imaging procedure is proposed in which three annular regions of retina are imaged in each phase. In the first two phases imaging is done by the aplanats and for the third stage a simple mobile can also be used. This imaging covers the whole retina, with some overlaps so that the images collected can be stitched together post that. In first two phases, sensors are specially designed which capture the 3D information of retina. The 3D reconstruction of complete retina from sensor data is discussed later in detail. A developed ray tracer is talked about which was used as the tool to work towards the aim. Though aplanats are aberration free, the light reflected from retina has to pass through the eye-lens which makes the aggregate system aberrant. After the 3D retina image is constructed, all the details can be identified but with slight blur. With appropriate signal processing techniques, a sharp 3D image of retina can be obtained.

Contents

Chapter 1

Introduction

Eye is an important organ in our body, which allows us to comprehend and navigate through the surroundings, defining our quality of life. We perceive upto 80% of all impressions by means of our sight [1]. But unfortunately, it is common to experience visual impairment due to various factors. Due to aging, lack of proper nutrition or hygiene, infections, or accidents cause poor and low vision or complete blindness to the sight. By studying the structure of the damage and by necessary medication, the lost sight can be brought back.

Ophthalmology is the study of the physical structure, functioning and diseases of the eye. Ophthalmologists, with the aid of technological advancements, have been able to look to the interiors of the patient's eye and accordingly diagnose and treat eye diseases and injuries. They are able to constantly monitor the progress and detect any development of abnormalities. A quality image of the interiors of the eye means a lot of information to the doctor about the patient. This thesis makes an attempt to propose a new imaging technique that captures the target features in the inside of the eye, giving a better and broader view.

1.1 Ocular Fundus

Fundus of the eye is the complete interior surface of the eye opposite the lens and includes the retina, optic disc, macula, fovea and posterior pole. An eye captures the light coming from the surroundings through an opening in front of it called the pupil. There is a transperant membrane in front of it called cornea and an accomodative eye lens behind it [8]. They focus the light entering the eye onto a curved screen at the back of the eye called retina. A two-dimensional image is formed on it. This screen is just analogous to that of a CCD sensor in a camera. It is a neuro-sensory tissue which converts the light to electrical impulses that our brain can understand and can create a visual perception.

The central region of the screen which is called a macula, is responsible for sharp, detailed central vision. A part of it called fovea, contains a high concentration of light-sensitive cells which give the detailed central, coloured vision. Also on the screen there is a region where no light falling on it can be captured, referred to as blind spot or the optic disc. It is the place where all the nerves in the eye exit and form the optic nerve after they leave. Optic nerve connects the eye to the brain. The region on retina between the macula and the optic disc is referred to as the posterior pole.

Photographing the fundus will record the retina, optic disc, macula and the blood vessels in it. The fundus can be photographed directly from pupil, which serves as the entry and exit for the illuminating light from fundus cameras.

1.2   Fundus Photography

Fundus photography involves capturing the entire back portion of the eye. It gives a record of the current ophthalmoscopic appearance of a patient's central and peripheral retina, macula, optic disc and the blood vessels in the retina. It helps the Ophthalmologists, who study the structure, functions and diseases of the eye, to follow, diagnose, and treat any eye diseases of the patient. They can be used to inspect anomalies associated to diseases of the eye and also to monitor their progress. It is vital for disease processes such as macular degeneration, retinal neoplasms, choroid disturbances and diabetic retinopathy [9].

In macular degeneration, the patient looses the center of the vision, causing bluriness. It is because of drying and deterioration of the macular region or due to leaky blood vessels growing under the retina. Diabetic retinopathy is caused due to the damage to the blood vessels in the retina, causing again a poor vision or complete blindness. Tumors on retina or retinal neoplasms can also badly affect the vision of a person.

A 2D photograph of the patient's eye fundus is used to study and identify abnormalities like swelling, leaking or dryness, also considering the symptoms exhibited by the patient. The fundus imaging is widely used for assessing these indicators quantitatively. The necessary surgery or vitamin medication is prescribed based on the follow up. Fundus Photography can be performed with colored filters or with specialized dyes including fluorescein and indocyanine green.

1.3   Fundus Camera

Fundus cameras are used for imaging the fundus. They have an intricate microscope along with a flash enabled camera. It's design is based on the principle of indirect Ophthalmoscope. A Fundus Camera provides a 2D upright, magnified view of the fundus. They are defined by the field of view they provide for viewing the retina which is the optical angle of acceptance of the lens used in them. They provide magnified view of 2.5x for field of views from 30° to 50° which are considered the normal angles of views. A narrower field of view of 15° provides a magnification of 5x and a wider field of view of 140° minfies the image by half [2]. Though the priniciple used in fundus cameras and Ophthalmoscopes is same, they differ in observation and illumination systems. Simultaneous stereo fundus cameras are also available to take images of both the eye at one exposure and place the images side by side on a single 35mm frame [3, 7].

Fundus Camera Optics

A fundus famera has two kinds of lighting, observation light and the flash light. The observation light is made annular by passing it through a series of lens and a doughut shaped aperture [10, 11]. It is then passed through the camera objective lens and through the cornea onto the retina. The reflected light from the retina passes through the un-illuminated hole in the light that has entered towards a low power telescopic eyepiece. To capture the image, a button is pressed and a mirror

interupts the illumination path while allowing the flash light to pass through the eye. Simultaneously another mirror redirects the light collected at telescopic eyepiece to the capturing medium which could be a film or a digital CCD.

The illumination system, the eye, and the imaging system have to be properly aligned and focused for the reflected light from retina to exit through the central, un-illuminated hole. When that happens, both the entering and exiting light paths will be independent resulting in minimal reflections of light source in the captured image. A Fundus Camera can also have a set of filters in front of the flash light and also astigmatic correction devices and diopter compensation lenses to correct the image being acquired.

1.4 Problems with Existing Fundus Cameras

Existing fundus cameras are mostly table-fixed, complex-to-operate, and have low image quality. They provide two-dimensional images for fundus or retina which are curved in shape, thereby distorting the peripheral information, even with wide field of view. Most of them have narrow field of view and retinal abnormalities outside the photographic field cannot be captured. They have shorter working distances in close proximity to the patient's eye resulting in patient's discomfort as well as greater potential for operator's error during alignment [12]. There can also be image artifacts and damage of patient's eye from over and under exposure [13]. Photobiological safety of lamps used for illumination also needs to be considered [14].

All of the fundus cameras use lenses for imaging. Lens are associated with aberrations and to compensate for them, a system of lens have to used. But that makes them very expensive and bulkier.

1.4.1 Disadvantages of and due to lenses

A lens is an optical device that focuses or disperses a light beam by means of refraction. A simple lens consists of a single piece of transparent material, while a compound lens consists of several simple lenses, usually arranged along a compound axis. An ideal lens should focus all the light from an object to form its image.

The current fundus cameras use a system of lenses to image the retina. In reality, a single lens does not form perfect images, and a lens always introduces some degree of distortion or aberration that makes the image an imperfect replica of the object. Careful design of the lens system for a particular application minimizes the aberration. Several types of aberration affect image quality, including spherical aberration, coma, and chromatic aberration.

Spherical Aberration

The shape of a spherical lens causes a problem called spherical aberration. In spherical aberration, parallel light rays that pass through the central region of the lens focus farther away than light rays that pass through the edges of the lens. The result is many focal points, which produce a blurry image as shown in Fig. 1.1.[4]. To get a clear image, all rays need to focus at the same point.
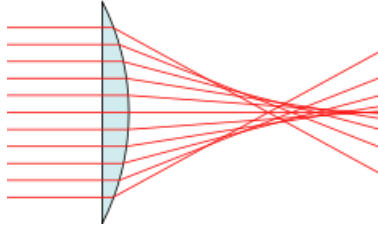
Figure 1.1: Spherical Aberration.

Coma Aberration

In optics (especially telescopes), the coma, or comatic aberration, in an optical system refers to aberration inherent to certain optical designs or due to imperfection in the lens or other components that results in off-axis point sources such as stars appearing distorted, appearing to have a tail (coma) like a comet as shown in Fig. 1.2.[5].
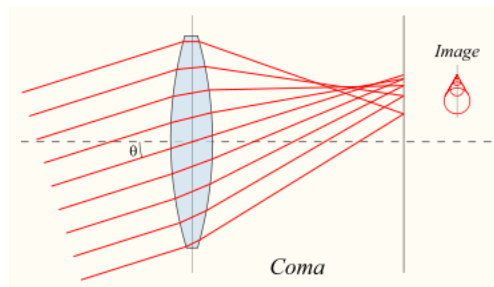
Figure 1.2: Coma Aberration.

Chromatic Aberration

Visible light is made of different colors. When visible light passes through a glass lens or a prism, it gets dispersed, or split, into its many colors. A lens focuses each color at a different point, causing a fringe of color to appear around bright objects as shown in Fig. 1.3.[6].
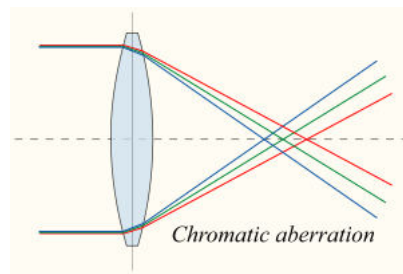
Figure 1.3: Chromatic Aberration.

Simple lenses are subjected to optical aberrations discussed above. In many cases these aberrations can be compensated for a great extent by using a combination of simple lenses with complementary aberrations. A compound lens is a collection of simple lenses of different shapes and made of materials of different refractive indices, arranged one after the other with a common axis.

However, compound lenses are very expensive and have low numerical apertures and thereby restrict the field of view of retina. Numerical aperture is a measure of how much light can be collected by an optical system. The NA is related to the acceptance angle, which indicates the size of a cone of light that can be accepted by the system.

1.5 Our Proposal

We aim to address the issues related to the image formation and aim to improve them by replacing the lens system in existing fundus cameras with aplanats. Aplanats are aberrations free and also provide with high numerical apertures. They are hollow like a tube and image with the phenomenon of reflection. Their properties allow us to image the peripherals of retina and also allow us to construct 3D images of it with specially designed curved sensors.

The following chapter is completely dedicated to the introduction of aplanats. Necessary definitions, and parameters that define the aplanat are talked about. Then major advantages of using aplanats over lens is mentioned which creates the foundation for why and how aplanats can be used to image the retina. Following that the imaging mechanism of aplanats is discussed. Then the derivation of aplanats' shape is talked about, including the principles and specifying equations of their contours. Then followed by are the special cases resulted when magnification is made to be either ±1.

In the third chapter of this thesis, we go to the properties of the unfolded aplanats. Again necessary definitions are mentioned and then inferences from the performed simulations are discussed. Major part of the chapter deals with the radiation analysis of aplanats. The results of the simulations in which light source is placed at different positions for imaging are discussed and inferences are made as to how positioning and different sizes of light source affect the illumination pattern on the receiver. Then limitations and trade offs of aplanats are discussed.

Introduction to the developed ray tracing program is made in chapter four. This was used as the tool to work towards the aim. The principle of ray tracing, and the principle of finding ray intersection points and finding resultant ray information, used in the program are discussed. Followed by that, different components or optical systems that can be created in the program are talked about. Then the performance details are mentioned.

In chapter five, complete details about the process of 3D imaging the retina are discussed. Starting with discussion on how an aplanat images the retina, we go to define how a sensor for an aplanat to capture 3D information of retina looks like. Then a three phase imaging procedure to image the retina upto 200° is proposed. Following that a detailed discussion about the process of construction of 3D image of retina using the specially designed curved sensors is given. Results obtained for three types of filters used is also provided.

The last chapter deals with the conclusion and further developments that can be made to refine the outputs presented in this thesis and also further challenges that have to be met are discussed.

Chapter 2

Aplanats

Aplanats belong to the near field optics. Near field optics is a branch of optics that considers configurations that depend on the passage of light to, from, through, or near an element with subwavelength features, and the coupling of that light to a second element located a subwavelength distance from the first.

2.1 Definition

Aplanat is a reflecting or refracting surface which is free from spherical, coma and chromatic aberrations. There are two types of aplanatic mirrors:
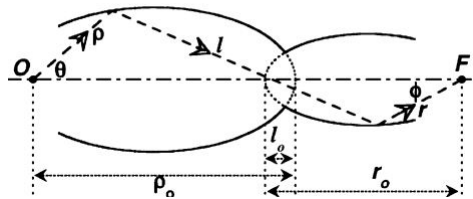
- Unfolded aplanat. Shown in Fig. 2.1.[17].

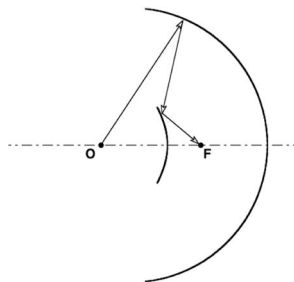Figure 2.1: Unfolded aplanat.

- Folded aplana. Shown in Fig. 2.2.[17].

Figure 2.2: Folded aplanat.

From Fig. 2.1, points 'O' and 'F' are its two focal points. The maximum value of θ is θ_o and that of ϕ is ϕ_o. The variables from the picture ρ_o, l_o, r_o, θ_o and ϕ_o are the five parameters that control the shape of the aplanat. The sine of θ_o and ϕ_o give us the entry and exit numerical aperture values, NA1 and NA2.

$$NA1 = \sin(\theta_o), \qquad NA2 = \sin(\phi_o).$$

Numerical Aperture value lies between 0 and 1. It defines the cone of light from a point source at focus, that is accepted by the optical system. From the Fig. 2.1, ρ defines the length of light ray between focal point 'O' and point of intersection on primary mirror, l defines length between intersection points on primary and secondary mirrors and r defines length between intersection point on secondary mirror and focal point 'F'.

The magnification of aplanat is given by the negative of ratio of entry to exit numerical aperture values

$$m = -\frac{NA1}{NA2} = -\frac{\sin(\theta)}{\sin(\phi)}$$

The second equality holds for every θ and corresponding ϕ of any light ray starting from point 'O' and falling on primary mirror.

2.2 Advantages over Lens

- Aplanat focuses divergent rays

- No spherical, coma, chromatic abberations

- High numerical apertures

- High radiation efficiency

- Non problematic monitoring and control

- For the same numerical aperture, the size of the lens will be very large

- All the light that enters the aplanat gets collected at the screen

2.3 Imaging Mechanism

Aplanat has a primary mirror and a secondary mirror. As shown in Fig. 2.1, the rays starting from the point source at 'O' which is one focal point, fall on the primary mirror first. Then get reflected and fall on the secondary mirror and the rays reflected by secondary mirror get collected at the other focal point at 'F'.

2.4 Derivation of Aplanatic Equations

The near-field unfolded aplanatic reflector contours can be derived by tracing rays from a point source to the focus and simultaneously satisfying [15]

- Fermats principle of constant optical path length (to eliminate spherical aberration)

- Abbes sine condition of constant magnification (to remove coma aberration)

- Snells law of reflection at raymirror intersections

2.4.1 Specifying equations

The aplanats mirror contours are specified based on following equations

- Axial stigmatism

$$\rho + r + l = \rho_o + r_o + l_o$$

- Sine condition

$$\sin\theta = m\sin u$$

- Reflection at primary mirror (i is the angle of incidence at primary mirror)

$$\frac{1}{\rho}\frac{d\rho}{d\theta} = -\tan i$$

2.4.2 Derivation

A complete derivation is not discussed here but only the gist. We consider the above equations and after some simplifications, we get a first order differential equation in terms of $\left(\frac{l_o}{\rho}\right)$ and its solution is the sum of any particular solution of it and an arbitrary multiple of the solution of the corresponding homogeneous equation

$$\frac{d}{d\theta}\left(\frac{l_o}{\rho}\right) = \left(\frac{l_o}{\rho}\right)F(\theta) + G(\theta)$$

$$F(\theta) = \frac{\sin\theta\{1 - \cos\theta - km - k\sqrt{(m^2 - \sin^2\theta)}\}}{\sin^2\theta - k(1 - \cos\theta)\{m - \sqrt{(m^2 - \sin^2\theta)}\}}$$

$$G(\theta) = -\frac{\sin\theta\{1 - \cos\theta + m - \sqrt{(m^2 - \sin^2\theta)}\}}{\sin^2\theta - k(1 - \cos\theta)\{m - \sqrt{(m^2 - \sin^2\theta)}\}}$$

Particular solution obtained by substituting a trial solution of the form $(A + B\cos\theta)$ is

$$\frac{l_o}{\rho} = \frac{1+k}{2k} + \frac{1-k}{2k}\cos\theta$$

The solution of homogenous equation is

$$\frac{l_o}{\rho} = C\exp\left\{\int F(\theta)d\theta\right\}$$

which can be evaluated using the substitution

$$\gamma = \cos\theta + \sqrt{(m^2 - \sin^2\theta)}.$$

Simplifying them will give us the primary mirror contour equation. From reversibility of the system the secondary mirror will have the same contour equation but 'm' replaced by '$\frac{1}{m}$'.

Primary mirror equation

$$\frac{l_o}{\rho(\theta)} = \frac{1+k}{2k} + \frac{1-k}{2k}\cos\theta + \frac{(r_o)(1+m)[\gamma(\theta)-1+m]^\alpha[\gamma(\theta)+1-m]^\beta[\gamma(\theta)(k+1)+(1-k)(1+m)]^{2-\alpha-\beta}}{4k\rho_o\gamma(\theta)m^\alpha(1+m)^{2-\alpha-\beta}}$$

where

$$k = \frac{\rho_o + r_o}{l_o}, \qquad \alpha = \frac{mk}{mk-1}, \qquad \beta = \frac{m}{m-k}, \qquad \gamma(\theta) = \cos(\theta) - \sqrt{m^2 - \sin^2(\theta)}$$

Secondary mirror equation

$$\frac{l_o}{r(\phi)} = \frac{1+k}{2k} + \frac{1-k}{2k}\cos\phi + \frac{(\rho_o)(1+M)[\delta(\phi)-1+M]^{\alpha'}[\delta(\phi)+1-M]^{\beta'}[\delta(\phi)(k+1)+(1-k)(1+M)]^{2-\alpha'-\beta'}}{4kr_o\delta(\phi)M^{\alpha'}(1+M)^{2-\alpha'-\beta'}}$$

where

$$M = \frac{1}{m}, \qquad \alpha' = \frac{Mk}{Mk-1}, \qquad \beta' = \frac{M}{M-k}, \qquad \delta(\phi) = \cos(\phi) - \sqrt{M^2 - \sin^2(\phi)}$$

2.5   Special Case

If $m = 1$, then primary and secondary mirror contours become as

$$\frac{\rho_o}{\rho} = \frac{\rho_o - r_o + l_o}{2l_o} + \frac{r_o - \rho_o + l_o}{2l_o}\cos\theta$$

and

$$\frac{r_o}{r} = \frac{r_o - \rho_o + l_o}{2l_o} + \frac{\rho_o - r_o + l_o}{2l_o}\cos\phi$$

These are polar equations of conics about a focus. In general one mirror is an ellipse and the other a hyperbola, but as special cases, both can be parabolas or one a sphere and the other plane.

If $m = -1$, then primary and secondary mirror contours become as

$$\frac{\rho_o}{\rho} = \frac{\rho_o + r_o + l_o}{2l_o} - \frac{\rho_o + r_o - l_o}{2l_o}\cos\theta$$

and

$$\frac{r_o}{r} = \frac{\rho_o + r_o + l_o}{2l_o} - \frac{\rho_o + r_o + l_o}{2l_o}\cos\phi$$

These are polar equations of conics about a focus, but in this case both mirrors are geometrically similar. Thus for a system with unit magnification ($m = \pm 1$) the mirrors must be conics.

Chapter 3

Properties of Unfolded Aplanats

Aplanats' internal surface needs to be perfectly reflective so as to have complete transfer of radiation power from light source to the screen. Materials like aluminium can be used to build aplanats. The internal surface should be finely polished and also the smooth surface has to follow the contour equations. The size of the aplanats can be of any order in length. It depends on the order of the parameters. A study of its properties and its radiation analysis have been made and are mentioned in this chapter.

3.1 Definitions

3.1.1 Thermodynamic Limit

The thermodynamic limit is given by the region on image plane with size of magnification (of aplanat) times the size of source. For an ideal aplanat, all the rays entering it must get concentrated within this region.

3.1.2 Numerical Aperture

It is the sine of the angle made by the rim of the aplanat with the optical axis at focus. There are two numerical apertures, entry NA and exit NA for unfolded aplanat. It indicates the cone of light accepted by the optical system.

3.2 Inferences from Simulations

Simulations were performed for a few designs of unfolded aplanats with lambertian disk source at one focus and receiver of radius 30mm on other focal plane as shown in Fig. 3.1. The Table 3.1 shows the results

We infer from the simulations that aplanat focuses only the light rays falling on the primary mirror. For some proper designs we can get 95% of the light that has entered the aplanat, focused near thermodynamic limit. The remaining 5% will be the losses.

Percentage of losses decreases with decrease in size of source and with increase in numerical apertures (NAs).

Table 3.1: Designs of unfolded aplanats.

| ρ_o (mm)	r_0 (mm)	l_o (mm)	Throat diameter (mm)	NA1	NA2	Power in aplanat (W)	Power in thermodynamic limit (W)	% of Losses
100	74.589	11.584	20.6514	0.9	0.66	0.77799	0.73263	5.83
100	96	36	23.994	0.9	0.66	0.79187	0.74697	5.67
102	97	13	23.9944	0.9	0.66	0.79192	0.74732	5.63
100	96	13	24.3006	0.9	0.8	0.80298	0.75791	5.61
102	97	13	24.3126	0.9	0.8	0.80276	0.75798	5.58
100	100	11.584	21.6326	0.9	0.66	0.79788	0.74919	6.01
113	93	7.5	14.00.22	0.9	0.66	0.80216	0.74185	7.52
104	99	16.5	29.9972	0.9	0.66	0.78185	0.73436	6.10
104	99	16.5	29.9972	0.9	0.66	0.78181	0.74143	5.16
100	80	12	22.332	0.94	0.95	0.87479	0.82972	5.15
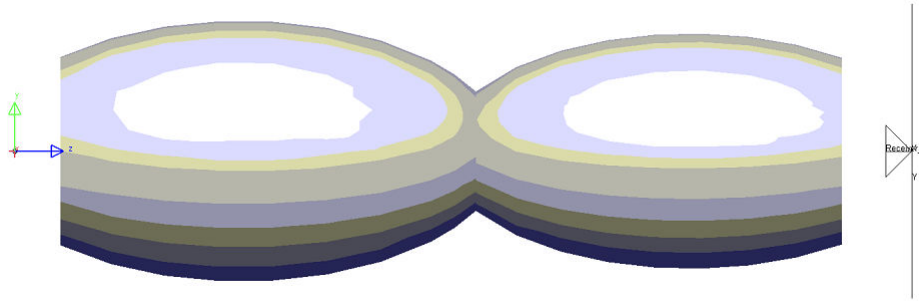
Figure 3.1: Unfolded aplanat with lambertian disk on left and receiver on right.

3.2.1 Moving the light source axially from focus

Simulations were performed by moving the light source axially from focus and the following setup was considered. The results are displayed in the Table 3.2

aplanat: ρ_o= 100mm, r_o= 96mm, l_o= 13mm, NAin= 0.9, NAout= 0.8

Source: radius= 0.4mm, thickness= 0.01mm, power= 1watt, lambertian disk

Receiver: radius= 30mm

Thermodynamic limit: radius=0.45mm

Throat length=24.3006mm

From the table we infer that when the light source is at the focus, we have large fraction of light that enters the aplanat to be lying in the thermodynamic limit. At other places we get a dip.

3.2.2 Moving the light source both axially and radially

Simulations were performed by moving the light source both axially and radially from focus and the following setup was considered. The results are displayed in the Table 3.3

aplanat: ρ_o= 100mm, r_o= 80mm, l_o= 12mm, NAin= 0.94, NAout= 0.95

Source: radius= 0.5mm, thickness= 0.01mm, power= 1watt, lambertian disk

Receiver: radius= 21mm

Thermodynamic limit: radius=0.495mm

Throat length=22.332mm

Table 3.2: Moving the light source axially from focus.

Coordinates of light source	Total power on receiver (W)	Power at thermodynamic limit (W)
(0,0)	0.80302	0.76161
(5,0)	0.67725	5.9e-6
(7,0)	0.56886	5.9e-6
(9,0)	0.49450	6.9e-6
(20,0)	0.28728	8.9e-6
(45,0)	0.05780	1.2e-5
(80,0)	0.42802	2.2e-5
(90,0)	0.90028	0.061
(-5,0)	0.63717	0.0032
(-7,0)	0.57544	0.001
(-9,0)	0.51862	4.9e-6

Table 3.3: Moving the light source both axially and radially.

Coordinates of light source	Total power on receiver (W)	Power at thermodynamic limit (W)
(0,0)	0.87479	0.82972
(1.5,0)	0.92135	0.08098
(3,0)	0.81973	0.01182
(3,1)	0.80386	0.02561
(4.5,0)	0.67305	0.00116
(4.5,1.3)	0.66093	0.01265
(80,0)	0.33956	7.63e-5
(90,0)	0.39963	5.37e-5
(94.73,0)	0.95099	7.1e-5
(100,0)	0.73187	9.44e-5
(120,0)	0.44216	0.000185
(130,0)	0.42769	0.000276
(145,0)	0.482201	0.000478
(163.68,0)	0.74895	0.000563

When we shift an LED radially, the intensity graph shifts by some distance.

3.2.3   Changing the LED size and moving it radially

Simulations were performed by changing the LED size and moving it radially from focus and the following setup was considered. The results are displayed in the Table 3.4

aplanat: ρ_o= 100mm, r_o= 80mm, l_o= 12mm, NAin= 0.94, NAout= 0.95

Source: thickness= 0.01mm, power= 1watt, lambertian disk

Receiver: radius= 21mm

Thermodynamic limit: radius=0.495mm

Throat length=22.332mm

Table 3.4: Changing the LED size and moving it radially.

Radius of source (mm)	Thermodynamic limit (mm)	Position of Source	Power in TL (W)
0.5	0.495	(0,0)	0.82972
0.5	0.495	(0,1)	3.57e-5
1	0.989	(0,0)	0.79194
1	0.989	(0,0.5)	0.16754
1	0.989	(0,0.8)	0.060512
1	0.989	(0,1)	0.019629
1.5	1.484	(0,0)	0.75016
1.5	1.484	(0,0.5)	0.23007
1.5	1.484	(0,0.8)	0.150222
1.5	1.484	(0,1)	0.10346
2	1.979	(0,0)	0.71227
2	1.979	(0,0.5)	0.25867
2	1.979	(0,0.8)	0.19838
2	1.979	(0,1)	0.16096

We can infer that as the size of source increases the power of light falling in thermodynamic limit increases for the same amount of radial shift. As the source is moved radially away from the axis the power of light falling in thermodynamic limit decreases.

3.3 Limitations and Trade Offs of Aplanats

One of the disadvantages is rays that do not fall on the primary mirror are not focused. Losses are due to rays passing through the throat directly, rays falling on secondary mirror directly and rays not going into the aplanat.

Also trade-off arises because lower power loss designs ,i.e., designs with a smaller waist-to-entry diameter ratio correspond to longer concentrators.

If 'm' is other than one with same ρ_o and r_o lengths, on the side with greater numerical aperture, some of the rays falling near the throat come back after going through two reflections in the primary mirror itself. This happens on the side with greater length, when 'm' is one with different lengths ρ_o and r_o.

The double reflection losses are of order $10^{-2}W$ out of $1W$ source. Even though they are near to insignificant losses, they can be avoided with some adjustments in the parameter values (Fig. 3.2).
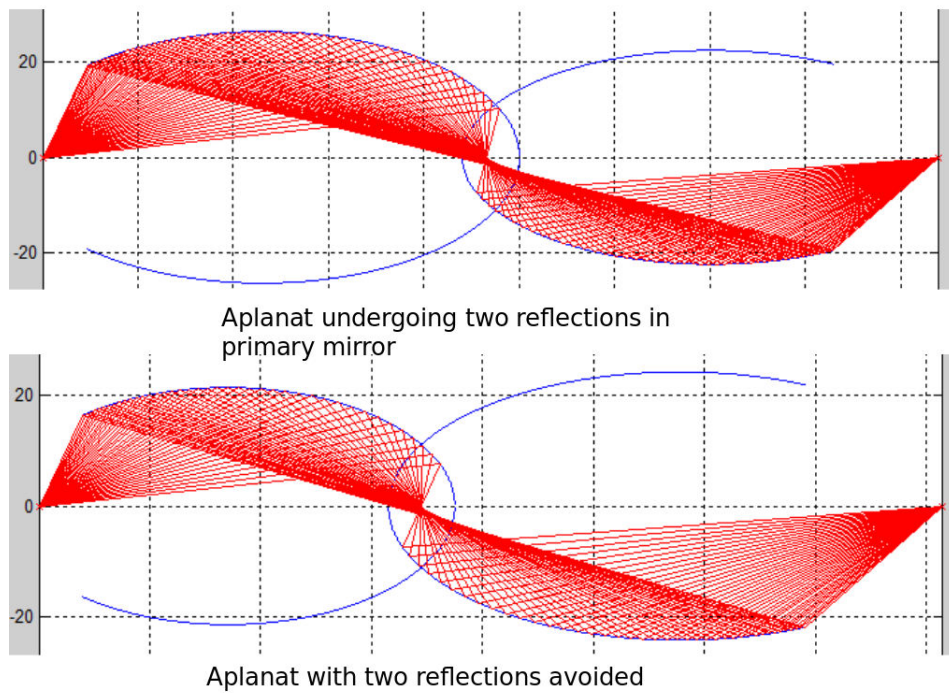
Aplanat undergoing two reflections in
primary mirror

Aplanat with two reflections avoided

Figure 3.2: Double reflections avoided with adjustments in parameters.

Chapter 4

Ray Tracer

The ray tracing program is written in Python, with assistance from the MATLAB toolbox Optometrika, using Object Oriented Programming concepts. Ray tracing program library implements analytical and iterative ray tracing approximation to optical image formation using Snell's laws of refraction and reflection. Currently the library implements lenses, aplanats, flat and curved screens, a realistic model of Human eye with accommodating lens and spheroidal retina. The library traces refracted rays, including intensity loss at the refractive surface.

Every optical system in the program is viewed as object. The simulation is setup by creating the objects and the user has to arrange the objects in the order of interaction by the rays from light source. The simulation will stop when all the objects in the order are met by the rays.

4.1 Principle of Raytracing

The light source is created by defining the starting point and direction for each ray coming from it. There are different shapes of light sources like linear, circular, square, pentagonal, hexagonal, spiral, random as shown in Fig. 4.1. These light sources can be made to be divergent, convergent, collinear, point source or a lambertian source. Wavelength, color and attenuation values can also be provided to each ray.
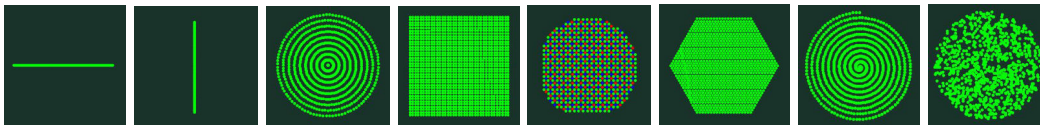

Figure 4.1: Different shapes of light sources. From left to right: linearY, linearZ, circular, square, pentagonal, hexagonal, spiral, random.

As mentioned before, each optical surface is viewed as an object and hence has a class of its own. The surface's geometric properties like diameter, height, width, medium, etc., are defined and its shape is constructed by generating a point cloud and creating a mesh over it. By giving the values for the geometric properties, one can get the desired shape for the optical surface as output.

The optical surfaces in the setup are created as objects by calling their corresponding classes. They are arranged in the order of interaction by the rays from light source. The whole setup is

viewed as one object. The ray bundle coming from the light source fall on the first surface and then undergo either reflection or refraction and create another ray bundle. These in turn undergo one of those phenomenons and fall on the next surface creating another ray bundle. This goes on until all the objects are met. Each of these ray bundles are also viewed as objects.

Each of these optical surfaces and ray bundle objects have functions defined in their classes which generate 2D or 3D point coordinates. All the objects' point coordinates are collected and 2D or 3D plots of the setup are plotted as desired.

4.1.1 Principle of finding ray intersection points

A ray is a straight line and so it bears a line equation with one unknown parameter. The optical surface has an equation and in order to find the point of intersection of the ray on it, we substitute the ray equation in the surface equation. Thereby getting a final equation with only one unknown parameter. Solving for it and substituting it back in the ray equation gives the coordinates for the point of intersection.

Depending on the phenomenon occurring near the surface, ie, either reflection or refraction, normals at the intersection points on the surface are calculated and appropriate formulae are applied to calculate the starting positions, directions, wavelengths, intensities, attenuations and colors of reflected or refracted rays. The rays that miss the surface are taken care of by excluding them from plotting.

4.1.2 Raytracing inside aplanat

Rays undergo two reflections inside the aplanat. The method used to find the intersection points is to solve for the point of intersection between the ray equation and the mirror contour equations. It is done in two parts first solve between the ray equation and the primary mirror contour equation then between the reflected ray equation and the secondary mirror contour equation.

Ray equation

$$\bar{r} + t.\bar{e} = 0$$

where $\bar{r}$ is the position vector of the starting point and $\bar{e}$ is the unit vector in direction of the ray. 't' is the unknown parameter, solving which will provide the intersection point.

Primary mirror contour equation

$$\frac{l_o}{\rho(\theta)} = \frac{1+k}{2k} + \frac{1-k}{2k}\cos\theta + \frac{(r_o)(1+m)[\gamma(\theta)-1+m]^\alpha[\gamma(\theta)+1-m]^\beta[\gamma(\theta)(k+1)+(1-k)(1+m)]^{2-\alpha-\beta}}{4k\rho_o\gamma(\theta)m^\alpha(1+m)^{2-\alpha-\beta}}$$

where

$$k = \frac{\rho_o + r_o}{l_o}, \qquad \alpha = \frac{mk}{mk-1}, \qquad \beta = \frac{m}{m-k}, \qquad \gamma(\theta) = \cos(\theta) - \sqrt{m^2 - \sin^2(\theta)}$$

Secondary mirror contour equation

$$\frac{l_o}{r(\phi)} = \frac{1+k}{2k} + \frac{1-k}{2k}\cos\phi + \frac{(\rho_o)(1+M)[\delta(\phi)-1+M]^{\alpha'}[\delta(\phi)+1-M]^{\beta'}[\delta(\phi)(k+1)+(1-k)(1+M)]^{2-\alpha'-\beta'}}{4kr_o\delta(\phi)M^{\alpha'}(1+M)^{2-\alpha'-\beta'}}$$

where

$$M = \frac{1}{m}, \quad \alpha' = \frac{Mk}{Mk-1}, \quad \beta' = \frac{M}{M-k}, \quad \delta(\phi) = \cos(\phi) - \sqrt{M^2 - \sin^2(\phi)}$$

But due to the complexity of the aplanat mirror contour equations, it was difficult to get a closed form equation to solve for the roots. So 'scipy.optimize.fsolve' algorithm was used. It returns the roots of the (non linear) equations defined by func(x)=0 given a starting estimate. This is a wrapper around MINPACK(FORTAN)'s hybrid optimizer, which itself is based on Powell-Optimization.

The initialization for the 'fsolve' optimizer decides the computation time and the accuracy of the calculation of point of intersection. The complete plot of primary and secondary mirror contours are shown in the Fig. 4.2. They form a closed surface. There will be utmost two intersection points with a line. For a given ray falling on either of the mirror surfaces, the point of intersection is selected heuristically.
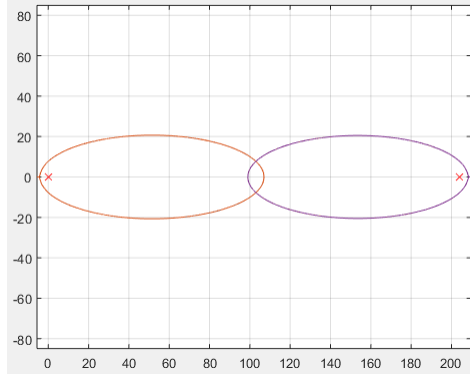

Figure 4.2: Plot of complete aplanat.

4.2 Optical Systems

An optical system (such as biconvex lens) is designed by defining the surfaces, here in this case using two convex surfaced 'lens' objects. All the optical surface classes are derived from a 'Surface' class. So they all have properties and methods of this class in common. Every surface will have location vector, rotation axis, rotation angle, orientation vector, material vector (which defines material in front and behind the surface by refractive indices) as common attributes. Functions to copy and rotate the object are common methods. The rotation happens in anit-clockwise direction given a rotation axis and a positive rotation angle.

4.2.1 Aplanat

Aplanat surface object is created as two objects: Primary mirror object and Secondary mirror object. We need to provide ρ_o, l_o, r_o, $NA1$, $NA2$ values along with location and material vector to define

the aplanat surface. In material vector, we define surface of aplanat to be 'mirror', surrounded by 'air'. The surface is created by rotating the contours of primary and secondary mirror about the optical axis (axis passing through both the foci). Figure 4.3 shows 2D and 3D plots of the aplanat.
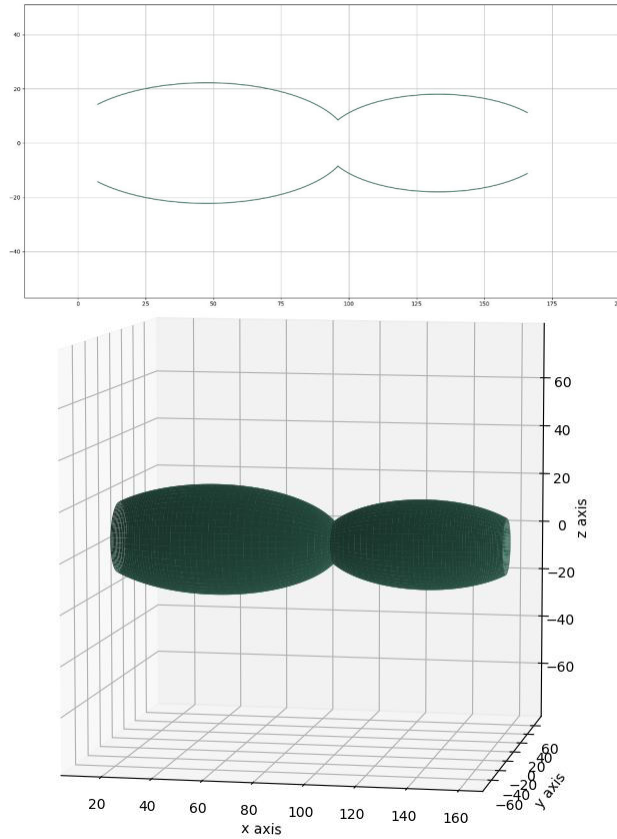

Figure 4.3: 2D and 3D plots of the aplanat surface.

4.2.2 Lenses

'Lens' implements a lens surface given by rotation of a conic curve. We need to provide values for diameter (both inner and outer), tangent sphere radius(R) and conic coefficient(k) along with location and material vector to define lens surface. Figure 4.4 shows the 2D and 3D plots of the lens. The conic curve is given by

$$z = \frac{\frac{r^2}{R}}{1 + \sqrt{1 - (1+k)(\frac{r}{R})^2}}$$

0 < k - oblate spheroid

k = 0 - sphere

-1 < k < 0 - prolate spheroid
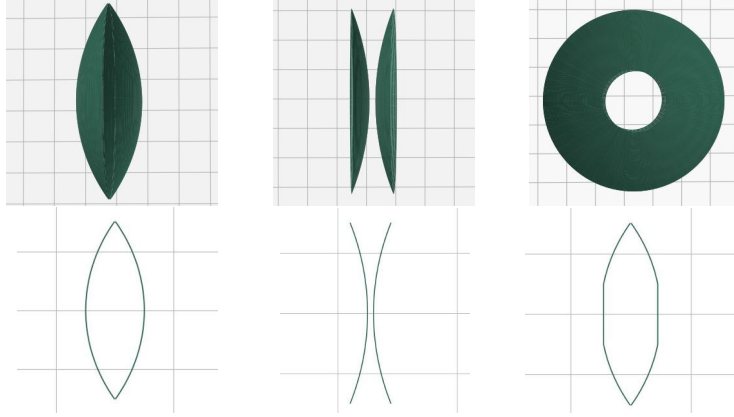
k = -1 - parabola

k < -1 - hyperbola

18

Figure 4.4: 2D and 3D plots of the lens surface. From left to right: convex lens, concave lens, annular convex lens.

4.2.3 Screen

Screen is basically a receiver or sensor which captures the light rays falling on it. It is divided into bins which define the resolution of image it captures. We can extract 2D histogram data containing the number of rays that fall in each bin of the grid also accounting for each ray's weight. Screen can be made to be of any shape, flat or curved. Figure 4.5 shows the 3D plots for flat and curved screen.
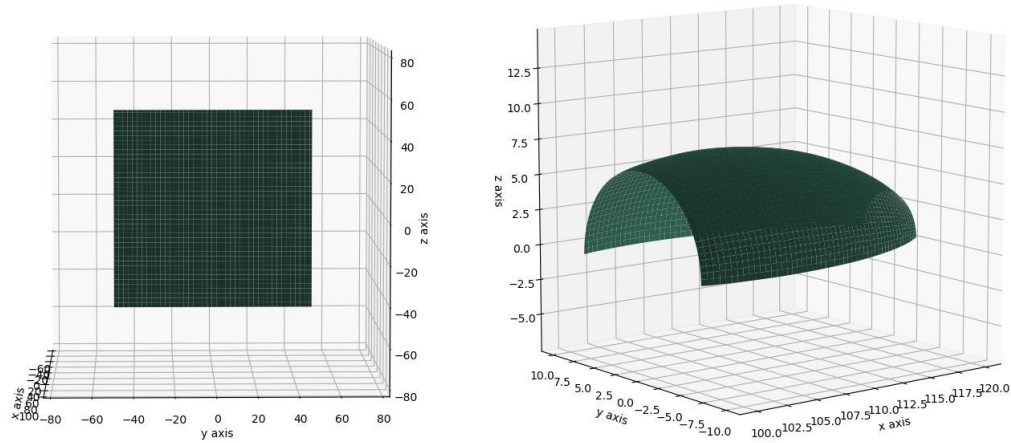

Figure 4.5: 3D plots of flat and curved screen.

4.2.4 Eye Model

Eye model implements human eye optics [18, 19]. The total depth of the eye is 23.93mm. The eye center of rotation was taken to be 13.3mm behind the corneal apex, which puts it 1.34mm behind the center of the eye [20]. High precision is immaterial since eye center of rotation actually moves by as much as 1 mm as the eye rotates, so the idea of the eye center of rotation is just an approximation. The retina shape was taken to be an oblate spheroid [21]. The retinal spheroid and lens slants were ignored here. Lens accomodation is modeled by its diameter variation assuming that the lens volume

19

is constant for all diameters [22].

The back lens surface was modeled by a paraboloid of revolution $x = \frac{y^2+z^2}{2R}$, its (constant) volume V is given by $\frac{\pi}{8}D^2h$, where h is the paraboloid height. Hence, $h(D) = \frac{8V}{\pi D^2}$ and $R(D) = \frac{\pi D^4}{64V}$. The front lens surface was modeled by a hyperboloid of revolution given by $x = \frac{R}{(1+k)}(1 - \sqrt{(1 - \frac{a(y^2+z^2)}{R^2})})$. The volume is $\frac{\pi}{8}D^2h(1 - \frac{h}{(6\frac{R}{(1+k)}+3h)})$, where h is the height of the hyperboloid from it apex to the cut of diameter D. Corresponding $h(D)$ and $R(D)$ formulas were obtained by solving a cubic equation, and its closed-from solution is implemented here.

Three examples were simulated to check with the accuracy of the eye model. First one was to demonstrate the optical model of the human eye. Second was to demonstrate the accommodation of the human eye by minimizing the retinal image. Third was to demonstrate the raytracing for rays originating inside the human eye. Figure 4.6 shows the 2D and 3D models of the eye and its interior regions.
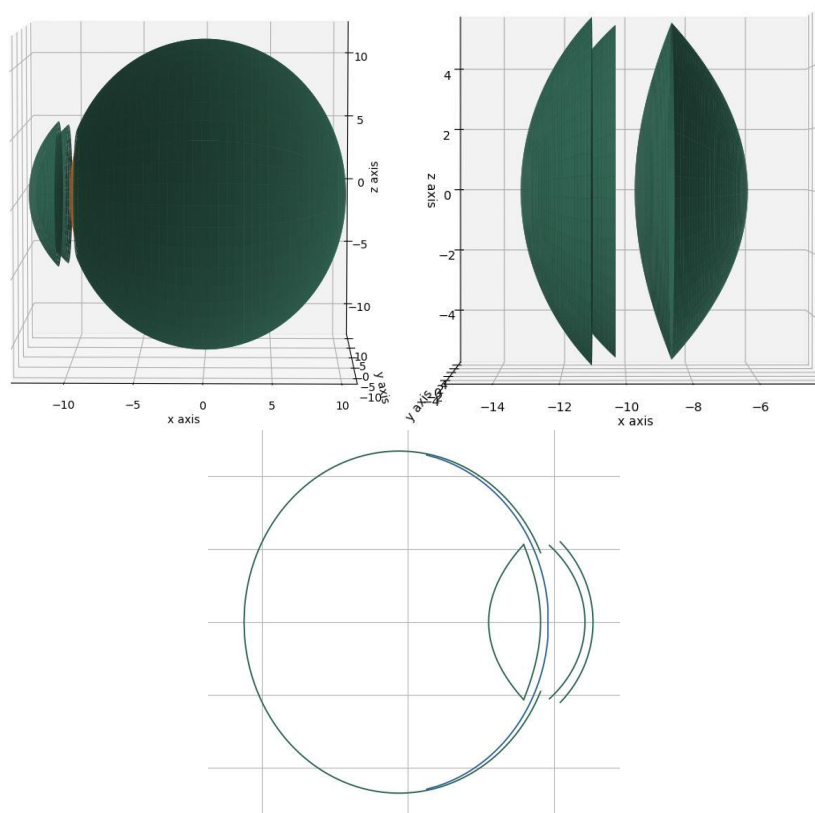

Figure 4.6: 2D and 3D plots of the eye and its interior regions. From left to right: 3D eye model, 3D eye lens, 2D eye model.

4.3   Performance of Ray Tracing Program

The library is very fast and compact. It was written using Python classes and is fully vectorized. It takes about 2 seconds to trace 100,000 rays through an external lens and the human eye (8 optical surfaces) on a 3GHz Intel Core i7 desktop. Tracing through user defined (general) surfaces is significantly slower due to iterative search of ray intersections with the surface.

Chapter 5

3D Imaging of Retina

The diameter of Pupil of the eye ranges from 2mm to 8mm. 2mm in bright light while 8mm in pure darkness. In order to take the picture of retina, we inject light through the Pupil and collect the light reflected by retina through the Pupil. In this procedure, the wider the Pupil is the easier it is to inject and collect light. So in general practices, sometimes patients are dosed with medicine which temporarily dilates the Pupil enabling the imaging process.

Our aim includes to image retina without any need of dilation of Pupil. So all the simulations performed contain the eye with minimum dilation which is 2mm diameter. To image the retina, light has to be injected through the Pupil. We assume that retina is uniformly illuminated. We intend to see how the image of retina is formed by the aplanat.

5.1 Imaging Points on Retina

In every simulation, the setup consists of the human eye model, an aplanat and a screen as shown in the Fig. 5.1. The Pupil has a 2mm diameter opening, one of the focal point of aplanat is placed inside the eye near the Pupil and the screen a little away from the second focal point of the aplanat.
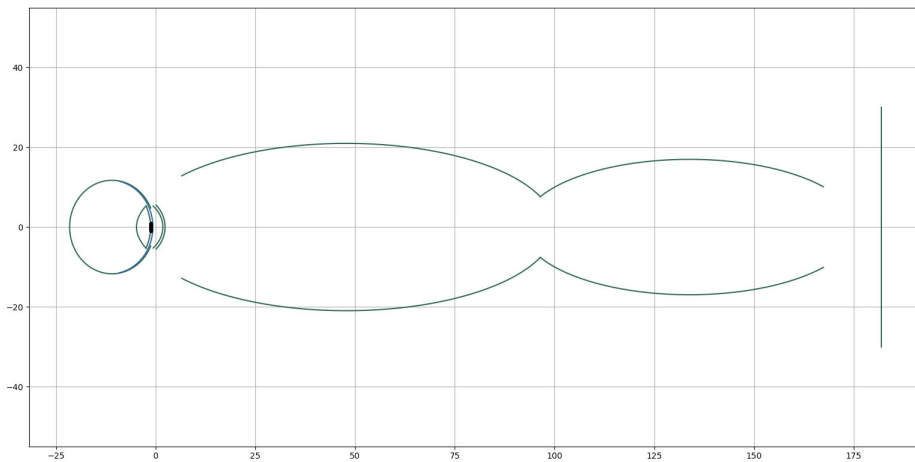

Figure 5.1: 2D plot of eye-aplanat-screen.

As shown in the Fig. 5.2 and Fig. 5.3, we can choose a point on retina as point source and send a cone of rays through the pupil onto the aplanat and see where its image has formed. The image will not exactly be a point as the eye lens will cause aberrations and so we get a plane instead as the image. From those figures we see, the image is formed at the tightest cross-section of the ray bundle falling on the screen.
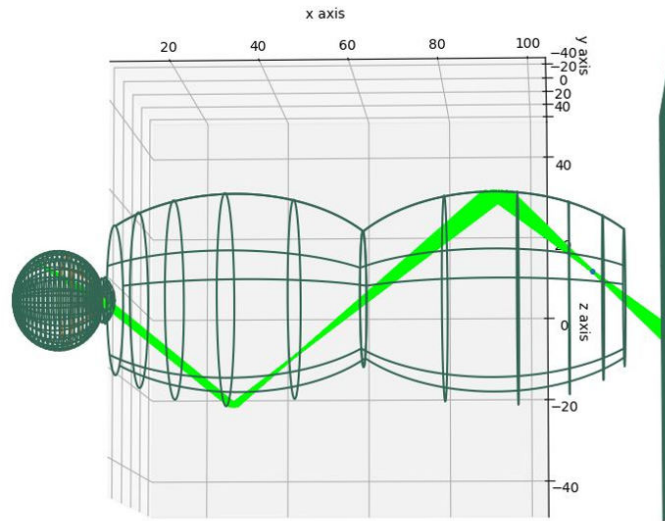

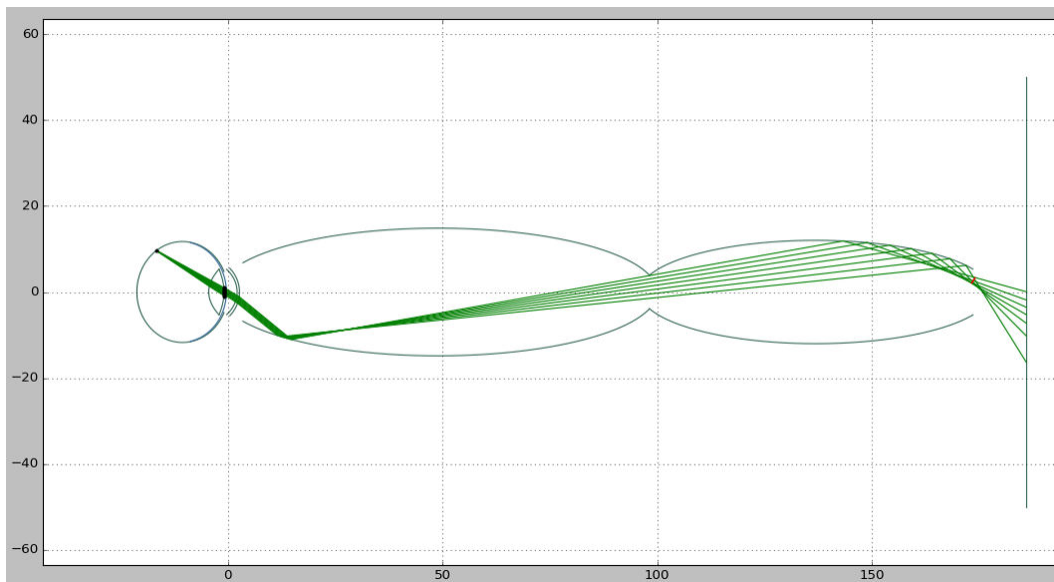Figure 5.2: 3D plot of eye-aplanat-screen.

Figure 5.3: 2D plot of eye-aplanat-screen.

The tight cross section is calculated by minimizing the standard deviation of the intersection points of the rays with the plane perpendicular to the average direction of all the rays. It is plotted in red color in the Fig. 5.3.

Convention used in simulations

If we imagine the eye model to be symmetrical around its optical axis and the center of the eye ball to be at the origin of the cartesian coordinate system, then a point on retina can be defined by the angle it makes with the x-axis at the origin and the angle between the z-axis and the perpendicular from that point on x-axis. In most of our discussions, we refer to points on retina by just the first parameter as we mostly consider points falling on xz-plane on the positive side of z-axis.

A single aplanat cannot cover or take the image of entire region of retina. There is always a hole in the middle, ie, the center part cannot be imaged as it is lost through the throat. Only a certain region between a lower angle and an upper angle on retina can be imaged. Let us consider the points on retina from 4° to 100°. Raytracing them through the aplanat, we see their images as red dots in Fig. 5.4. For the aplanat shown in that figure, the angles 4° to 46° (from first dot till cluster) form non-cluster points and the rest of the angles form clusters. The cluster at the end is formed because the points on retina at those angles are all falling near the edge of the primary mirror. They appear to be of same height to the aplanat.
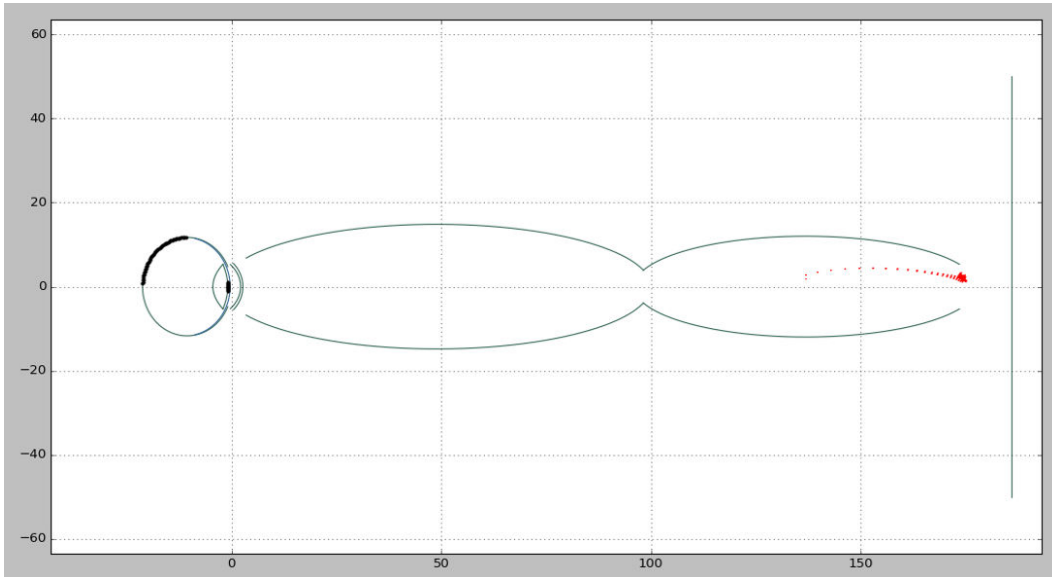

Figure 5.4: Images of retina points from 4° to 100°. Black dots are the retina points and red dots are the image points. First red point from left is formed by point on lowest angle on retina.

We infer that, if we put a sensor along those non-clustered points we can image the corresponding points on retina. In addition, the smoother the surface of such image points, the easier it will be to place a sensor along it.

5.2   Effect of Change of Aplanat Parameters

The angles on retina that form the non-cluster images imply that those regions on retina can be imaged. In this section, the effect of changing the parameters of the aplanat on image points is discussed.

- By changing the $NA1$ or $NA2$, we are just increasing or decreasing the acceptance cone of the aplanat. If there is a decrease in the $NA1$, the peripheral angles on retina cannot be imaged.

- By changing the l_o, there is a shift in the lower and upper angle of points on retina being imaged. By increasing the l_o value, the lower angle and the upper angle on the retina that can be imaged by the aplanat will increase in value.

- By changing the ρ_o and r_o, the distribution of the images of points from lower angle to upper angle on retina changes. With increase, distribution of the images of points near lower angle get wider and of points near upper angle get closer. With decrease, the opposite tends to happen.

5.3 Bringing Image Points outside Aplanat

The only way to bring the image points outside the aplanat is by using lenses. But the resultant image points of the lens system may not have a smooth surface and this is not the big limitation. The image points near the rim of secondary mirror are formed by very steep rays and making the lens image those points with out adding aberrations is very difficult. Also we are using aplanats because they are aberration free and adding lens will defeat the very purpose.

5.4 Our Proposal

Since a single aplanat cannot cover the complete retina, we require more than one phase of imaging. In order to reach higher angles, we propose to image in total three phases.

First phase

In this phase, we image the peripheral angles on retina, from 26° to 100° using the aplanat $(rhont, lnt, rnt, NA1, NA2) = (70, 18, 70, 0.99, 1)$. The Fig. 5.5 shows images of uniformly selected angles on retina. The Fig. 5.6 shows the x-coordinate of image points vs angle plot. Now sampling the x-coordinates uniformly, we can get the corresponding angles. The Fig. 5.7 shows the angles for which the images are uniformly spaced along with blue normals. The Fig. 5.8 shows the zoomed pictures of image points, eye, and curve fitting the image centers. The sensors for this aplanat will be placed on the surface formed by rotating that curve. The Fig. 5.9 shows the 3D plot of eye, aplanat and its sensor.

Second phase

In this phase, we image angles in the middle region on retina, from 6° to 40° using the aplanat $(rhont, lnt, rnt, NA1, NA2) = (120, 6, 120, 0.99, 1)$. The Fig. 5.10 shows images of uniformly selected angles on retina. The Fig. 5.11 shows the x-coordinate of image points vs angle plot. Now sampling the x-coordinates uniformly, we can get the corresponding angles. The Fig. 5.12 shows the angles for which the images are uniformly spaced along with blue normals. The Fig. 5.13 shows the zoomed pictures of image points, eye, and curve fitting the image centers. The sensors for this aplanat will be placed on the surface formed by rotating the that curve. The Fig. 5.14 shows the 3D plot of eye, aplanat and its sensor.
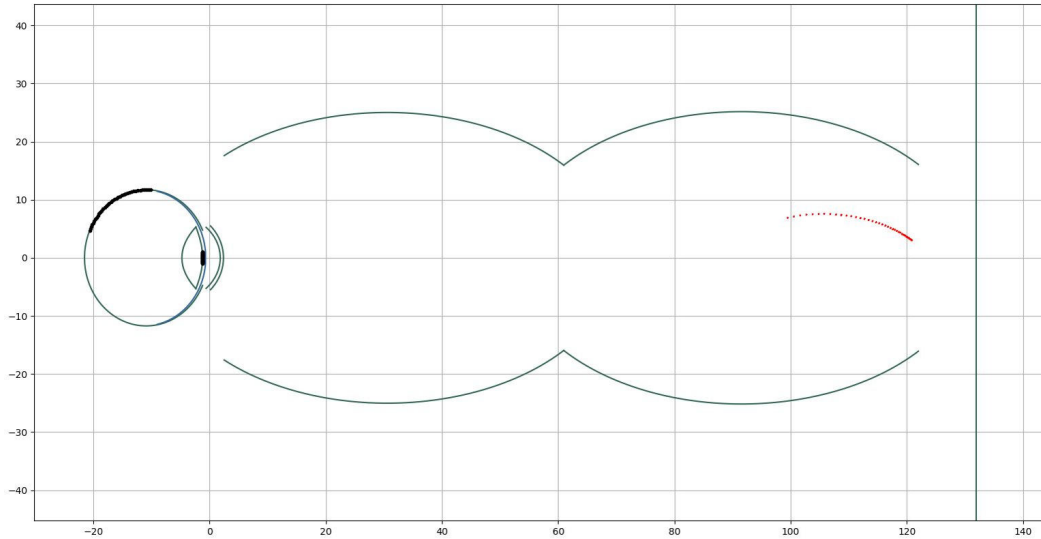
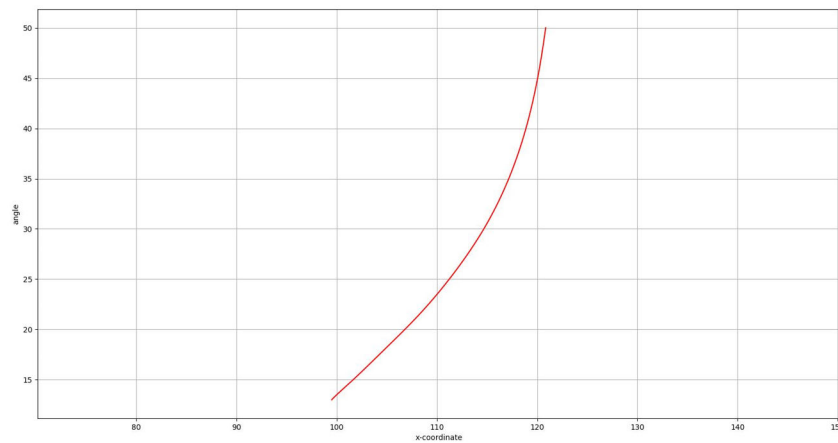Figure 5.5: 2D plot showing image points of uniformly placed points on retina.

Figure 5.6: Plot of x-coordinate of image points vs angle of points on retina.

Third phase

In this phase, we image the center part of the retina, from 0deg to 10deg using mobile or some other simple camera.

It should be noted that there are three sensors being used, one for each phase. The 3D images collected from these three phases are then stitched to form the complete 3D image of the retina.
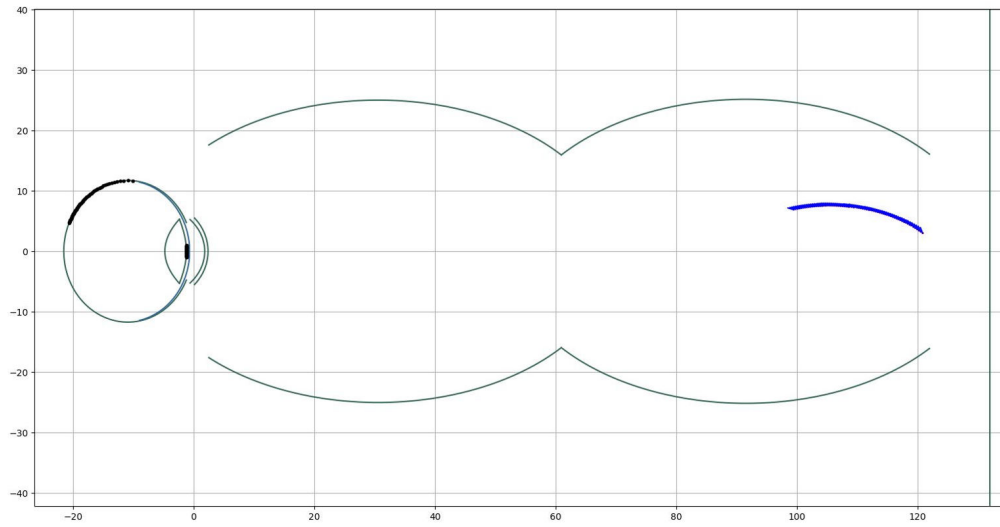
Figure 5.7: 2D plot showing the angles for which the images are uniformly spaced, with blue normals.
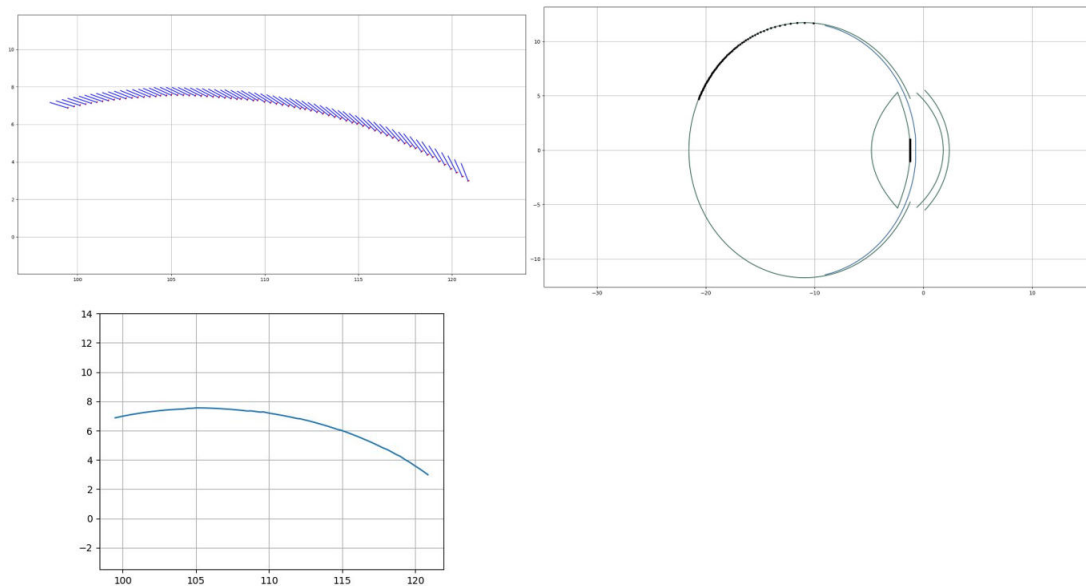

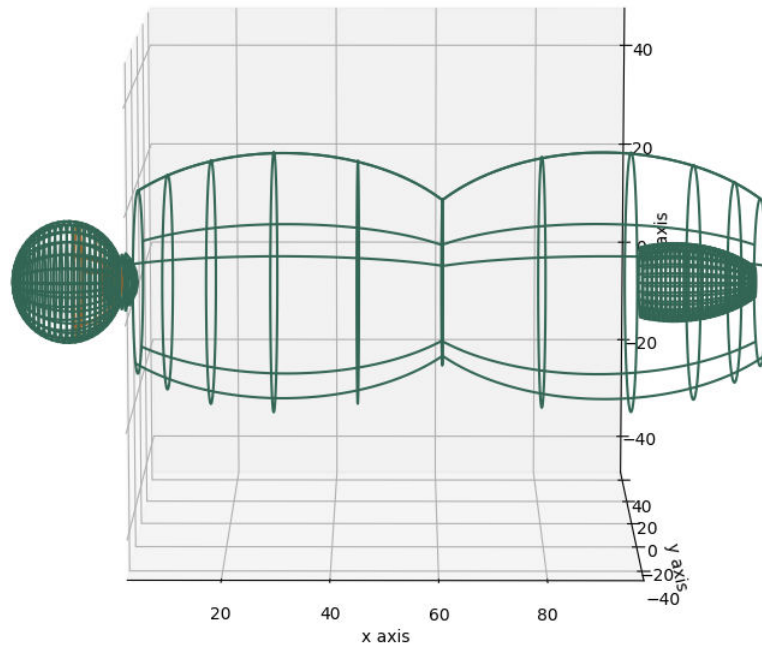Figure 5.8: Zoomed pictures of image points, eye, and curve fitting the image centers.

Figure 5.9: 3D plot of eye, aplanat and its sensor.

Figure 5.10: 2D plot showing image points of uniformly placed points on retina.

Figure 5.11: Plot of x-coordinate of image points vs angle of points on retina.

Figure 5.12: 2D plot showing the angles for which the images are uniformly spaced, with blue normals.

Figure 5.13: Zoomed pictures of image points, eye, and curve fitting the image centers.

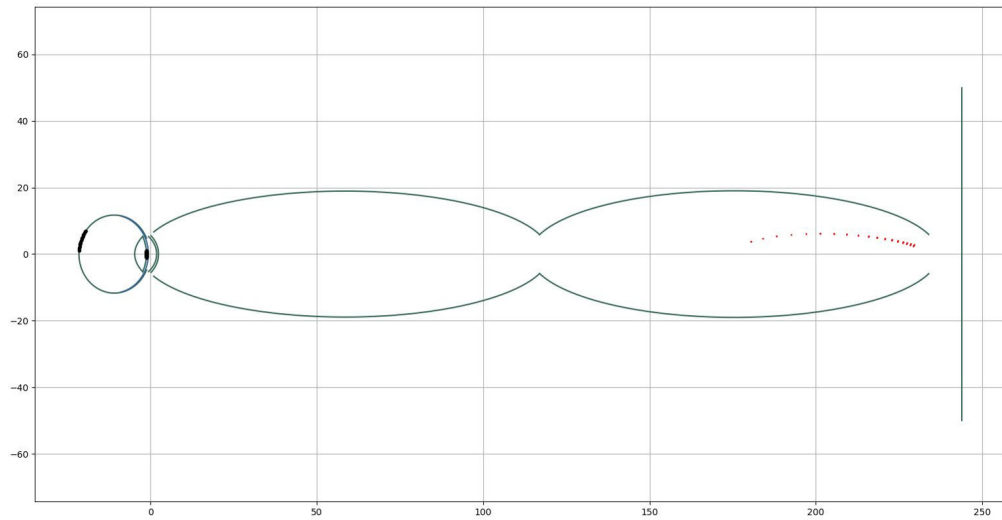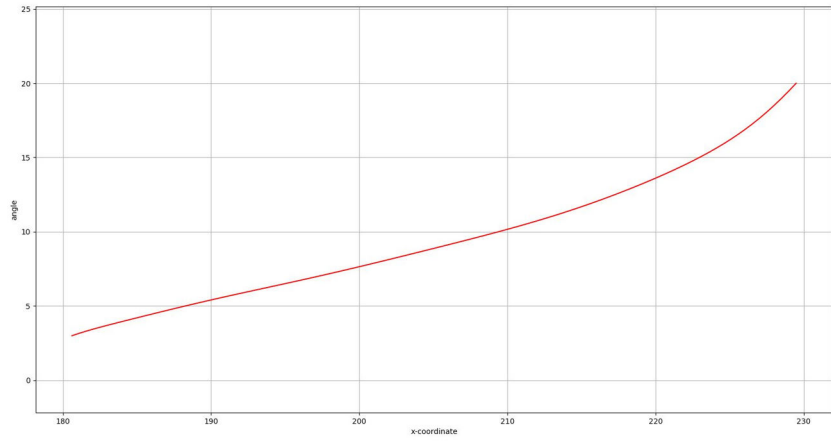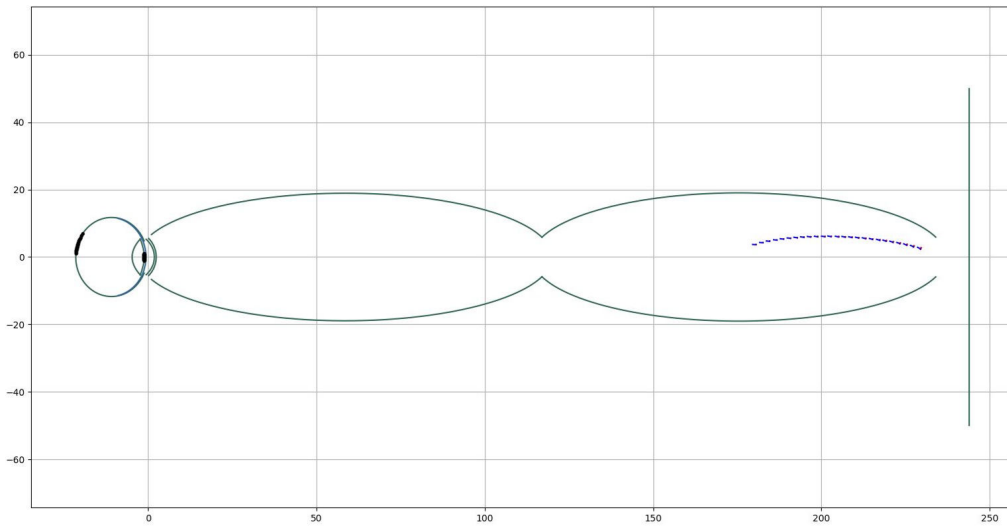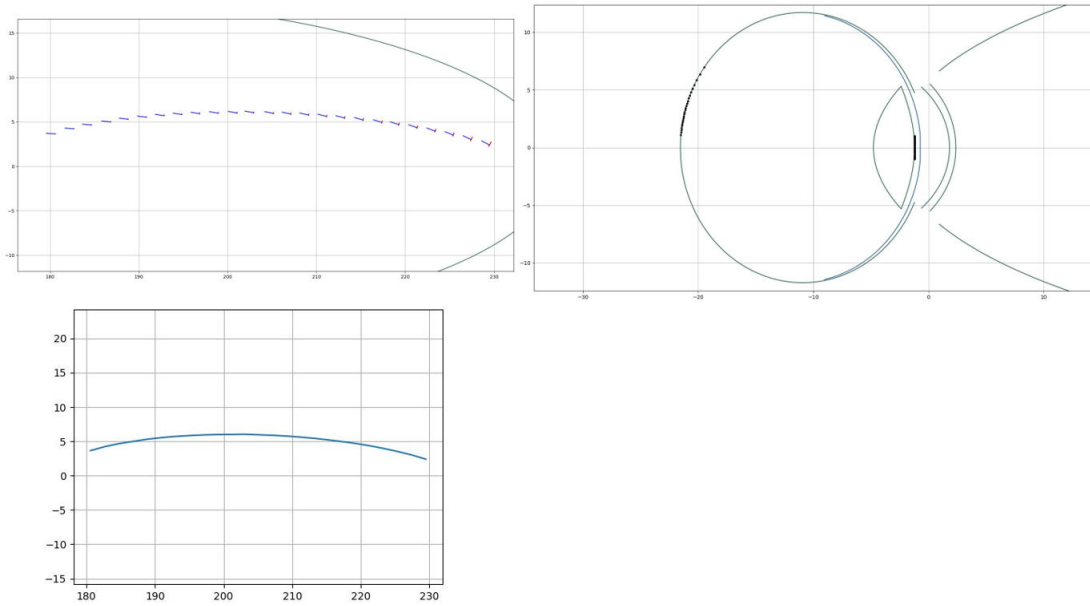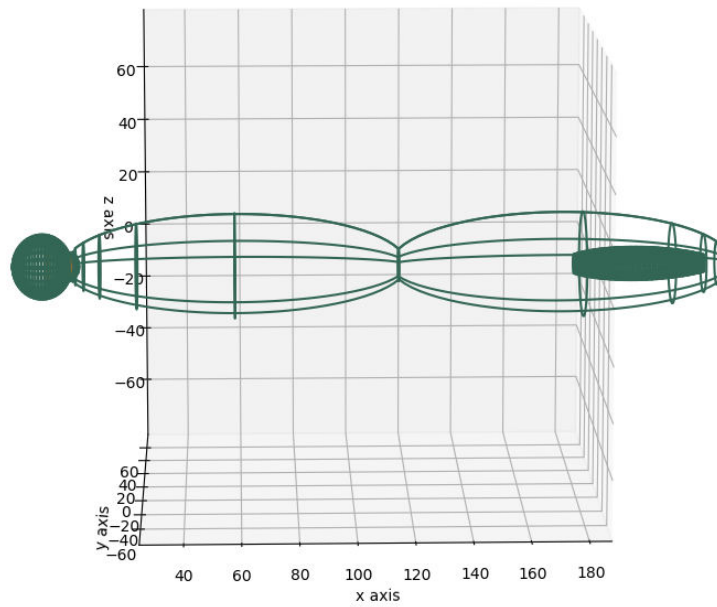Figure 5.14: 3D plot of eye, aplanat and its sensor.

29

5.5   Increasing the Resolution

The sensor we are using is 500micron x 500micron in size. The resolution is dependent on placing of the sensors and the number of sensors. The are placed in such a way that a point on retina is not predominently imaged in more than one sensors. At the extreme periphery of the retina vertically, if we consider some number of points within a degree and simulate it on the small sensor, we can get a plot of point-angle vs sum-intensity of each point falling on the sensor. From the plot, we get a peak at some angle and by taking half bandwidth of the graph we can know how many image points we can have within that degree vertically at that region on retina. It should be noted that the sensor will image the peak angle point along with contributions from other points. Now if we consider points horizontally within a degree around the peak angle and simulate it on the sensor, we can get a plot of the same graph which will be symmetric this time. By taking half bandwidth of the graph, we can know how many image points we can have within that degree horizontally at that region on retina. The number of image points constitute the number of sensors and we can know the spacing based on how many are to be fit within a degree. We do the same exercise at all other degrees and obtain the number of sensors to be placed to image those regions. Also we repeat the whole process for both the aplanats. We take one full degree for aplanat from first phase and a half degree for aplanat from second phase.

The Table 5.1 below shows the exercise done for five single vertical degrees on retina using the aplanat from first phase $(rhont, lnt, rnt, NA1, NA2) = (70, 18, 70, 0.99, 1)$. The sensor positions are the x-coordinates of their centers. Within each degree, 400 points were taken and from each point 1500 rays were traced. Here the angles are measured from pupil.

Table 5.1: Vertical angle vs intensity table for aplanat from first phase.

Angles in deg.	Sensor positions	Peak Angle	Half Bandwidth (per deg.)	Number of sensors vertically
13.5-14.5	100.560	14.04637	0.006	166
20.5-21.5	107.784	21.099	0.0055	181
30.5-31.5	115.203	31.082	0.008	125
40.5-41.5	119.177	41.39223	0.025	40
48.5-49.5	120.710	49.27945	0.035	28

The Table 5.2 below shows the exercise done for five single horizontal degrees on retina around the peak angles from table Table 7.1 using the aplanat from first phase. Within each degree, 400 points were taken and from each point 1500 rays were traced. Here the angles are measured from pupil.

Table 5.2: Horizontal angle vs intensity table for aplanat from first phase.

Peak Angle	Sensor positions	Half Bandwidth (per deg.)	Number of sensors horizontally
14.04637	100.560	0.11	9
21.099	107.784	0.11	9
31.099	115.203	0.11	9
41.39223	119.177	0.11	9
49.27945	120.710	0.11	9

The Fig. 5.15 shows the angle vs intensity plots for aplanat from first phase. Both the images

are the same except for the zoom in the second image. The first row is for the vertical angle and the second row is for the horizontal angles in both the images.
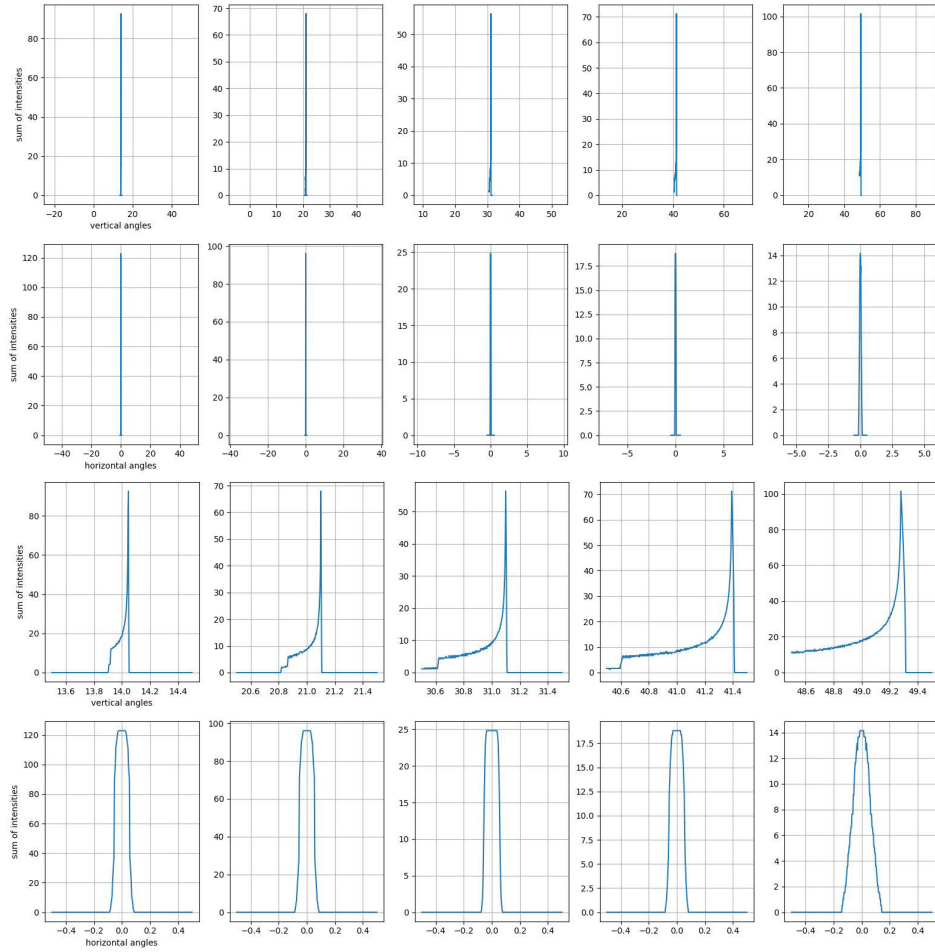

Figure 5.15: Angle vs intensity plots for aplanat from first phase.

The Table 5.3 below shows the exercise done for five single vertical half-degrees on retina using the aplanat from second phase $(rhont, lnt, rnt, NA1, NA2) = (120, 6, 120, 0.99, 1)$. The sensor positions are the x-coordinates of their centers. Within each half-degree, 400 points were taken and from each point 1500 rays were traced. Here the angles are measured from pupil.

Table 5.3: Vertical angle vs intensity table for aplanat from second phase.

Angles in deg.	Sensor positions	Peak Angle	Half Bandwidth (per half-deg.)	Number of sensors vertically
3.3-3.7	182.31	3.513534	0.004	250
6.3-6.7	194.956	6.539599	0.003	333
10.3-10.7	211.178	10.6198	0.002	500
14.3-14.7	221.274	14.50852	0.005	200
16.3-16.7	225.521	16.4995	0.006	166

The Table 5.4 below shows the exercise done for five single horizontal degrees on retina around the peak angles from table Table 7.3 using the aplanat from second phase. Within each degree, 400

31

points were taken and from each point 1500 rays were traced. Here the angles are measured from pupil.

Table 5.4: Horizontal angle vs intensity table for aplanat from second phase.

Peak Angle	Sensor positions	Half Bandwidth (per deg.)	Number of sensors horizontally
3.513534	182.31	0.11	9
6.539599	194.956	0.11	9
10.6198	211.178	0.11	9
14.50852	221.274	0.11	9
16.4995	225.521	0.11	9

The Fig. 5.16 shows the angle vs intensity plots for aplanat from second phase. Both the images are the same except for the zoom in the second image. The first row is for the vertical angle and the second row is for the horizontal angles in both the images.
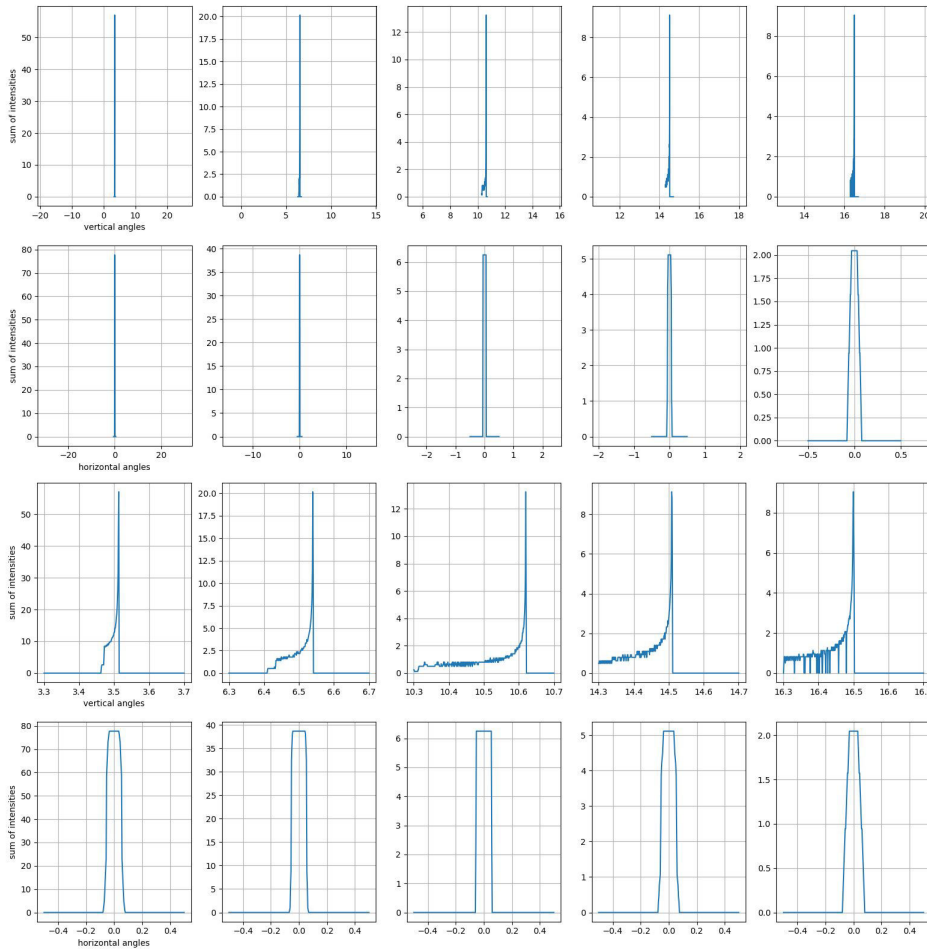

Figure 5.16: Angle vs intensity plots for aplanat from second phase.

5.6 Obtaining the Digital Painted Model of Retina

A very high resolution 3D retina is constructed using the Meshlab software. This is considered as the digital version of painted retina to be imaged. A hemi-spheroidal shaped, high density point cloud is created and normals are calculated at each point. Then "screened Poisson Surface Reconstruction" filter is applied on it to create a mesh over the point cloud. The resultant mesh is cleaned and the face-normals and vertex-normals are normalized. Following that we project a high-resolution 2D image of retina onto the current mesh thereby giving a texture to it. Then sampling the mesh will give the retina coloured, high density point cloud. The Fig. 5.17 shows six views of 3D retina model constructed.
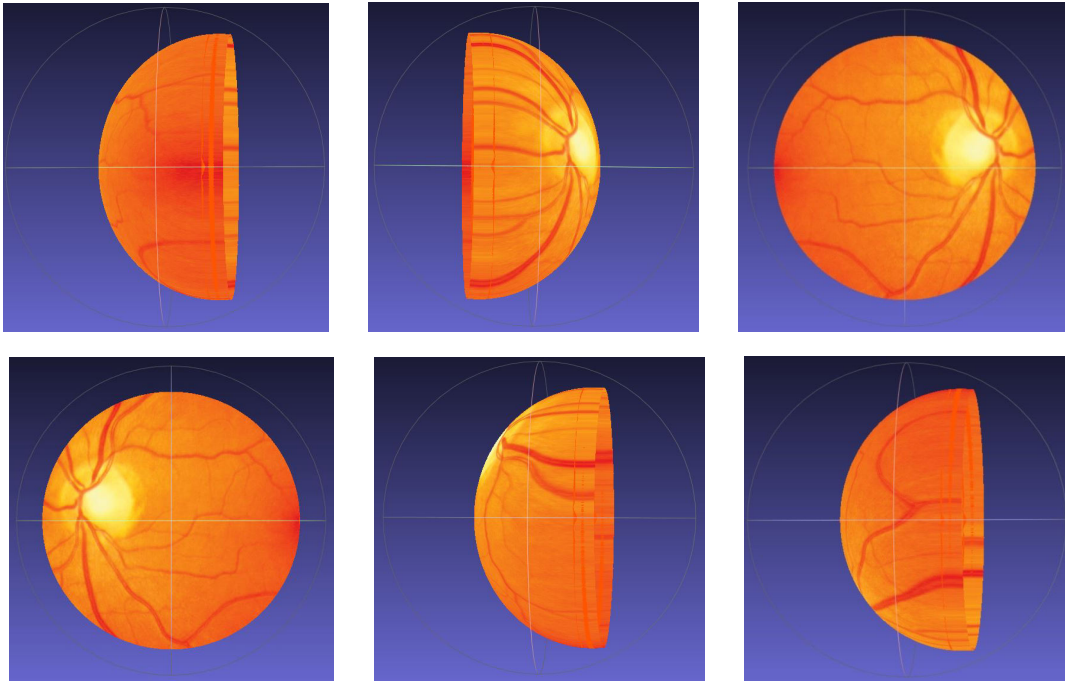

Figure 5.17: Different views of digital painted retina model constructed from Meshlab.

5.7 Mapping and Placing the Sensors

Mapping of sensors to retina points is important to know which region of retina is being imaged by a sensor. For mapping, in the ideal case, we first simulate all retina points onto the 3D sensor. Then, a 500micron x 500micron sensor is placed in the region hit by the rays and using angle vs intensity graphs for that sensor, the peak angle obtained will be mapped to it. The placing of sensors will be such that no two sensors will image the same retina point.

In the case of simulations, the process to get the mapping for a point on retina to its corresponding imaging sensor is same for both aplanats, which is as follows. The simulation setup consists of eye, aplanat and its complete sensor as shown in the Fig. 5.9 and Fig. 5.14. Only the points on the retina on x-z plane on the positive side of z-axis are considered. Now each point acts as a point source and ray tracing is performed. A table is created which stores the origin angle, 3D coordinates of

intersection point and intensity value of every ray that falls on the sensor.

For a 500micron x 500micron patch considered anywhere on complete sensor perpendicular to the plane of the points on retina, with the help of the table, we can collect the rays falling in the region same as the patch. Then we can plot point-angle vs sum-intensity plots and know the peak angle point for that patch. It means that for the patch at that position will image the peak angle point on retina. This way we can get the mapping for all points on retina by varying the patch position and plotting the graphs with the help of table.

All such sensors will be placed in the plane of that longitude and the retina points on the plane will be mapped to them accordingly. With assistance from the vertical angle vs intensity graphs, sensors are placed such that no two sensors image the same retina point. After that, considering points on retina perpendicular to x-z plane at every peak angle point within a degree and simulating on the peak angle point's sensor, we can get how many points we can have horizontally at that region on retina. The whole set can then be rotated around the optical axis, 9 sensors per degree, to obtain the complete discretized 3D sensor. The mapping will also be rotation symmetric.

5.8   3D Image Reconstruction

5.8.1   Principle used for 3D image Construction

A 500micron x 500micron sensor receives rays from a patch of points on retina. The value of the sensor, then, is the sum of all the intensities contributed by each point in the patch. Which means that, if we know the contributions made by each point on to that sensor, we can find the value collected by it. By forming the weight matrix and using rotation symmetry, we can find the values for remaining sensors in same latitude.

Consider the points on retina on x-z plane on positive side of the z-axis and their corresponding sensors. For each sensor, to calculate the contribution from neighboring longitude retina points onto it, can be done in two ways. The first method is to consider rays from the neighboring retina points onto that sensor and calculating their contribution. Second method is to place another sensor on its side and to look at the contribution on it from the existing longitude points, to get the relative weights. This second method was used in simulations to construct the weights for a patch.

5.8.2   Patch weights construction

Consider the same setup described above. 22 other sensors are placed on either side of a center sensor. It should be understood that, relatively, we are looking for the contribution from retina points on 22 longitudes on either side of the central longitude. For each of those 45 sensors, with the help of the table that was created for mapping and which stores the ray information, rays falling on it are searched. For each ray, information about its origin angle and intensity value are available. This information is then clubbed into two arrays for each sensor such that one has all the unique angles and the other containing corresponding sums of intensities.

From this exercise, the relative locations of points on the retina will be known and their summed intensities that fall on the center sensor. So we will have 45 sets of two-arrays. The angle made by each sensor from the center one will give us the contribution from the retina points on the longitude that makes the same angle with the central longitude. And the unique angles for each sensor

mean the points on retina at those particular angles on its corresponding longitude. So the patch boundaries are the minimum unique angle to maximum unique angle longitudinally and latitude wise, the angles made by the extreme sensors with center, on either side.

The unique angles serve as the positions and the corresponding summed intensities serve as the weights. Each sum-intensity array is scaled to values between 0 and 1. This is done by dividing the whole array by its maximum value. The Fig. 5.18 shows an example plot of how a weight patch looks like. The 45 lines correspond to each of the 45 sensors and the points above the flat sensor imply the intensity or weight value at those locations. The weight patch is then placed on the coloured 3D retina model. The weights are then multiplied with the R, G, B intensities of the retina points at those locations and summed to get a 1x3 RGB vector. This colour value is then assigned to the point mapped to the center sensor. The patch can then be used to find the RGB intensity values for other sensors on the latitude by rotating the patch around the optical axis on the 3D retina model. This procedure is done for all the sensors along the longitude plane to reconstruct the 3D retina image.
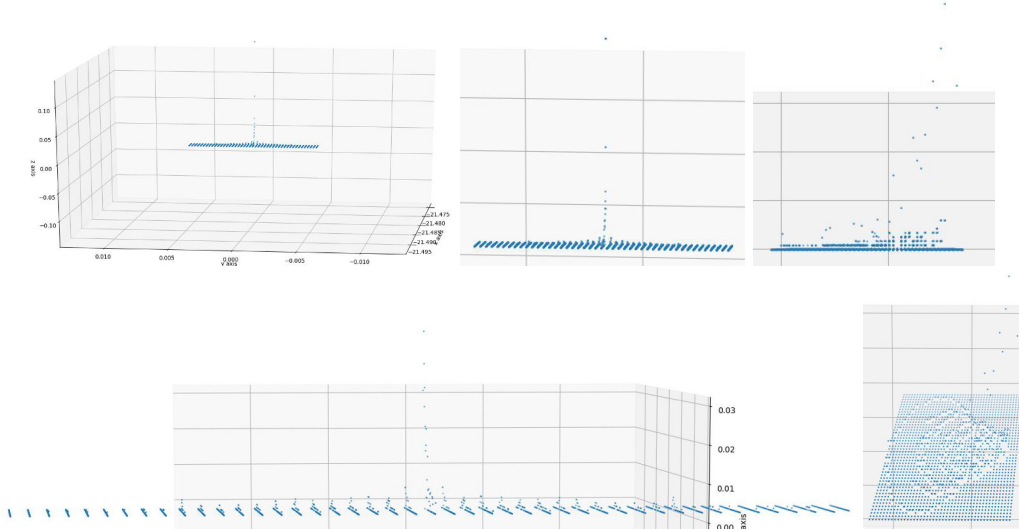

Figure 5.18: Different views of an example weight patch constructed.

5.8.3 3D image constructed using mean filter

In the 3D retina model, the number of points falling under the weights patch were not enough in number to perform the point wise multiplication. So just the mean of the RGB intensities of the retina model points falling under the patch boundaries was taken. It was then assigned to the corresponding sensors mapping point. Figure 5.19 shows the 3D images reconstructed using mean filter. The blurring is due to equal weightage given to all the angles in the patch.
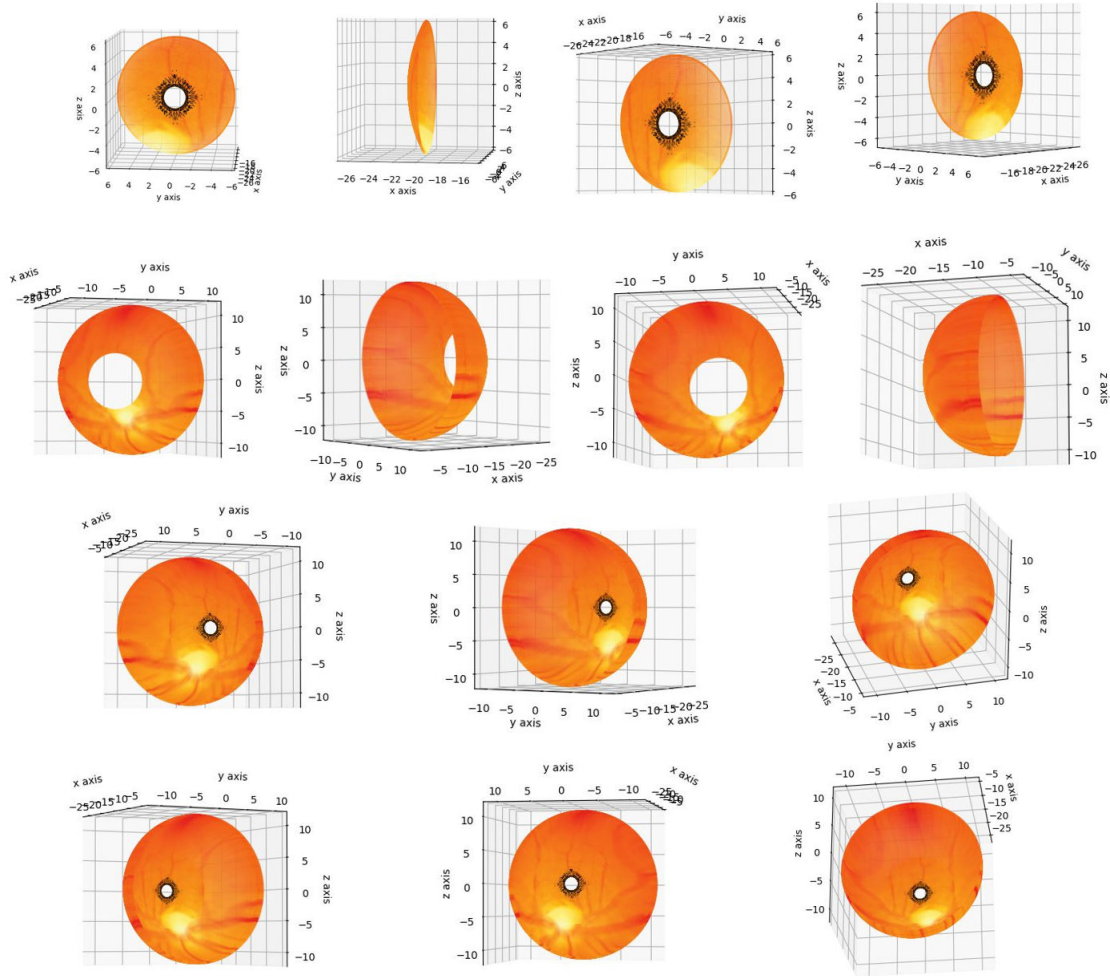
Figure 5.19: 3D images reconstructed using mean filter. From top to bottom: First row 3D images generated by the aplanat from second phase. Second row 3D images generated by the aplanat from first phase. Third and fourth rows are different views of the merged 3D images from both the aplanats.

5.8.4 3D image constructed using delta function

Ideal 3D retina image reconstruction would be when there is no contribution from the neighboring points on the sensor except from its mapped point. It means that the weight patch is like a delta function. So within the patch boundaries, the intensity of point on retina model closest to the mapped point's location is given to the mapped point. Figure 5.20 shows the 3D images reconstructed using delta function . There is no blurring in this case.
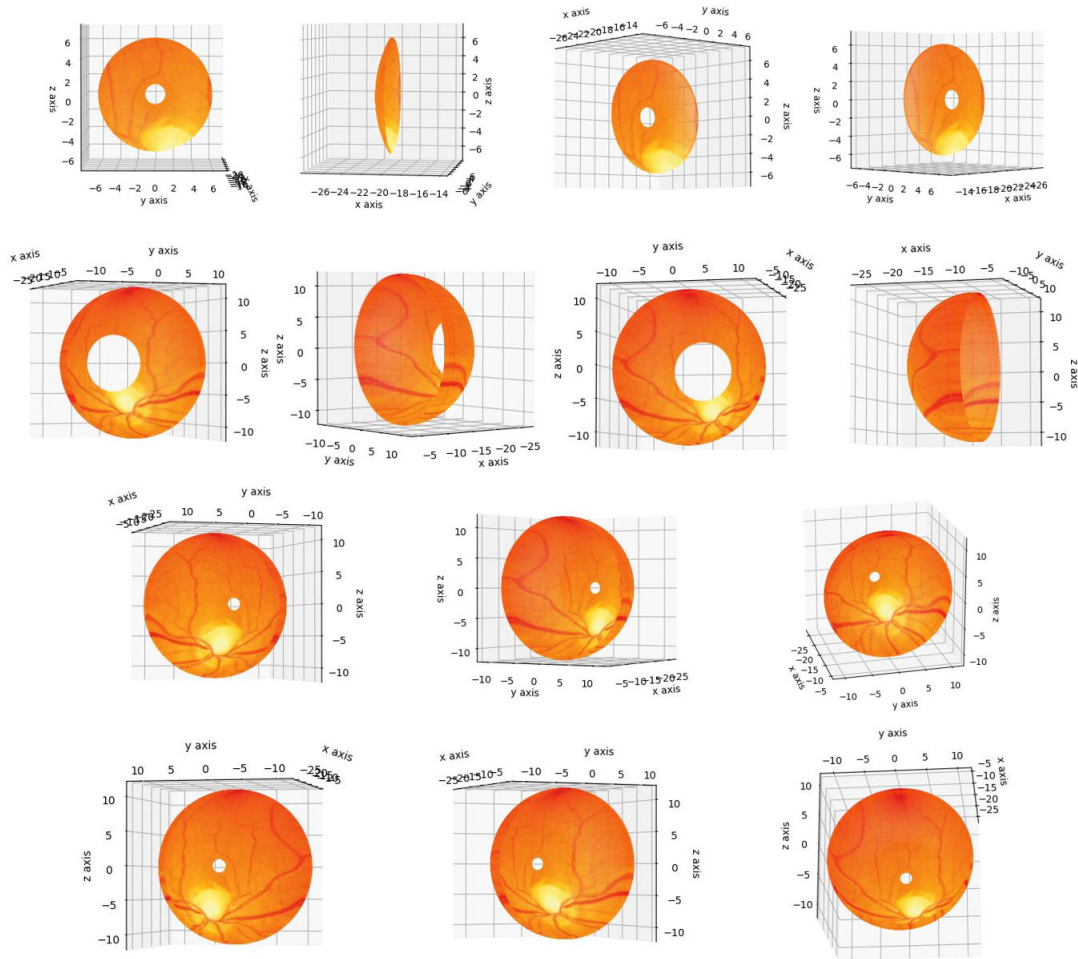
Figure 5.20: 3D images reconstructed using delta function. From top to bottom: First row 3D images generated by the aplanat from second phase. Second row 3D images generated by the aplanat from first phase. Third and fourth rows are different views of the merged 3D images from both the aplanats.

5.8.5 3D image constructed using weighted patch and interpolation

Since there was scarcity of points within the patch boundaries to perform pointwise multiplication, new points were created using interpolation. All model points under the patch were considered for interpolation of each point on the weight patch. At the location of each point on the weight patch, the RGB intensities were taken proportional to the distances and were added. Then at those locations, the weights and the RGB intensities were multiplied and summed up. That is then assigned to the sensor's corresponding mapping point. Also since the weight matrix was large, it was binned to bring it to a lower size. Figure 5.21 shows the 3D images reconstructed using weighted patch and interpolation. Some blurring is still left due to binning and scarcity of points and aberrations due to eye lens. That can be dealt with Signal Processing.
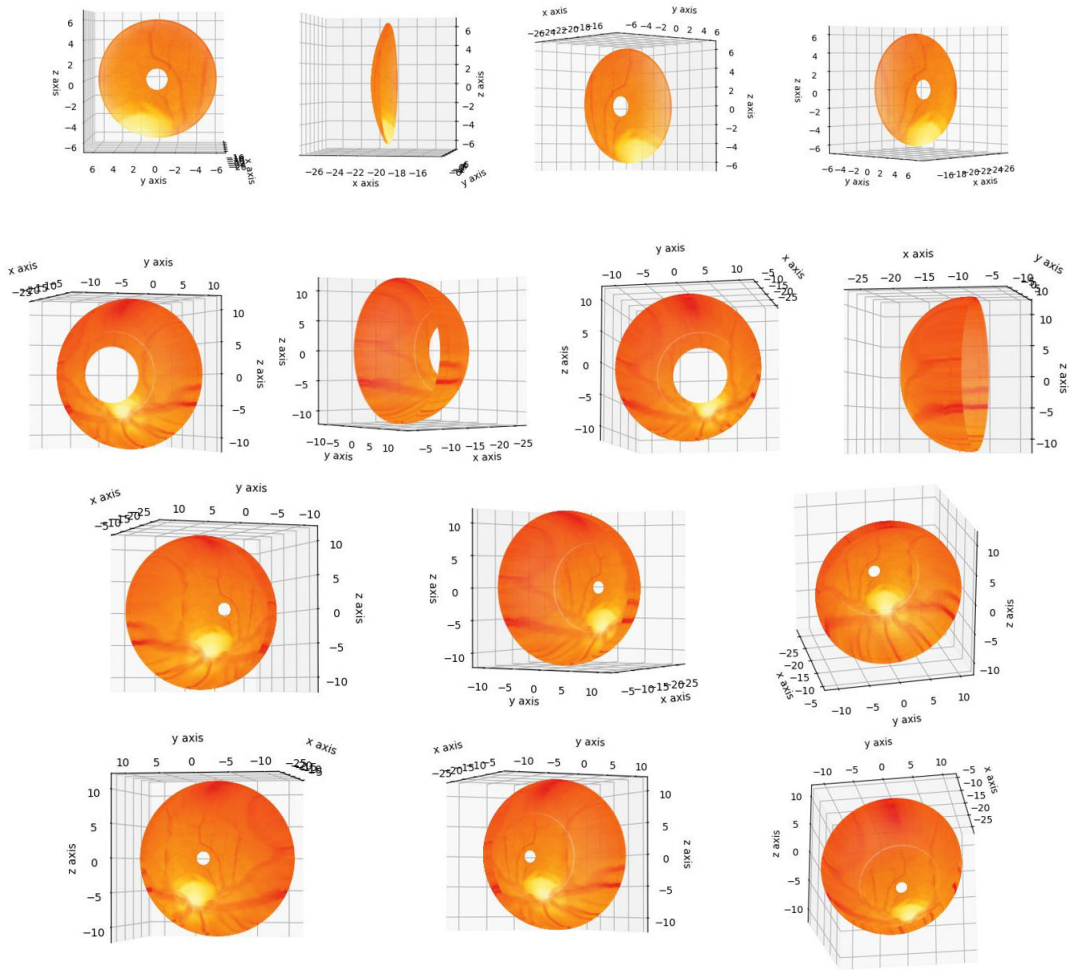
Figure 5.21: 3D images reconstructed using weighted patch and interpolation. From top to bottom: First row 3D images generated by the aplanat from second phase. Second row 3D images generated by the aplanat from first phase. Third and fourth rows are different views of the merged 3D images from both the aplanats.

Chapter 6

Conclusion and Future Developments

This thesis makes an effort to shed light on a new path of imaging with the use of aplanats. The developments required to move further closer to our actual aim are mentioned in this chapter.

6.1 Conclusion

Aplanats have the capability to collect highly diverging rays due to their high numerical apertures. This feature can be used to image the peripheral regions of the retina. Aplanats are advantageous than lenses in many ways and they are aberration free. They use reflection phenomenon to image and have 95% of radiation efficiency. Their properties allow us to construct a 3D image of retina with specially designed curved sensors.

The developed ray tracing program is fast at computation and is fully vectorized. All the simulations were performed using this as the tool. The pupil diameter of eye model in every simulation was fixed at 2mm. Assumption was made that retina is uniformly illuminated and that it reflects light back uniformly. The optical systems in the simulations eye, aplanat, sensors were all aligned along the optical axis and are rotation symmetric.

In this thesis, an attempt has been made to demonstrate using simulations, the 3D reconstruction of retina in three phases of imaging using aplanats. In the first phase, using the wide field of view aplanat, we image the regions lying between 26° and 100° angles on retina. In the second phase, using the narrow field of view aplanat, regions lying between the angles 6° and 40° will be imaged. In the third phase, a simple imaging system like a mobile or simple camera will be used to image angles from 0° to 10° on retina.

The design of sensors for the first two phases is provided and the technique used in simulations for constructing the 3D model of retina was also discussed. The weight patch created for every sensor which contains the contribution from the neighboring points of its mapped point looks like a near delta function. The results include reconstructed 3D images of retina from 0° to 100° angles, giving us a total of 200° field of view. Blurring to some extent is present in the results which can be dealt with Signal Processing techniques.

6.2 Future Developments

6.2.1 Cutting and masking the aplanats

Since both aplanats used in two phases have high numerical apertures, there is a possibility that the patient's nose might obstruct while imaging. As shown in Fig. 6.1, only the region on primary mirror falling between the rays will be utilised. Therefore, the extra region can be cut off for the convinience in imaging. Also we can put a black mask around the rim of the aplanat to avoid external light from entering the aplanat besides light coming from pupil.
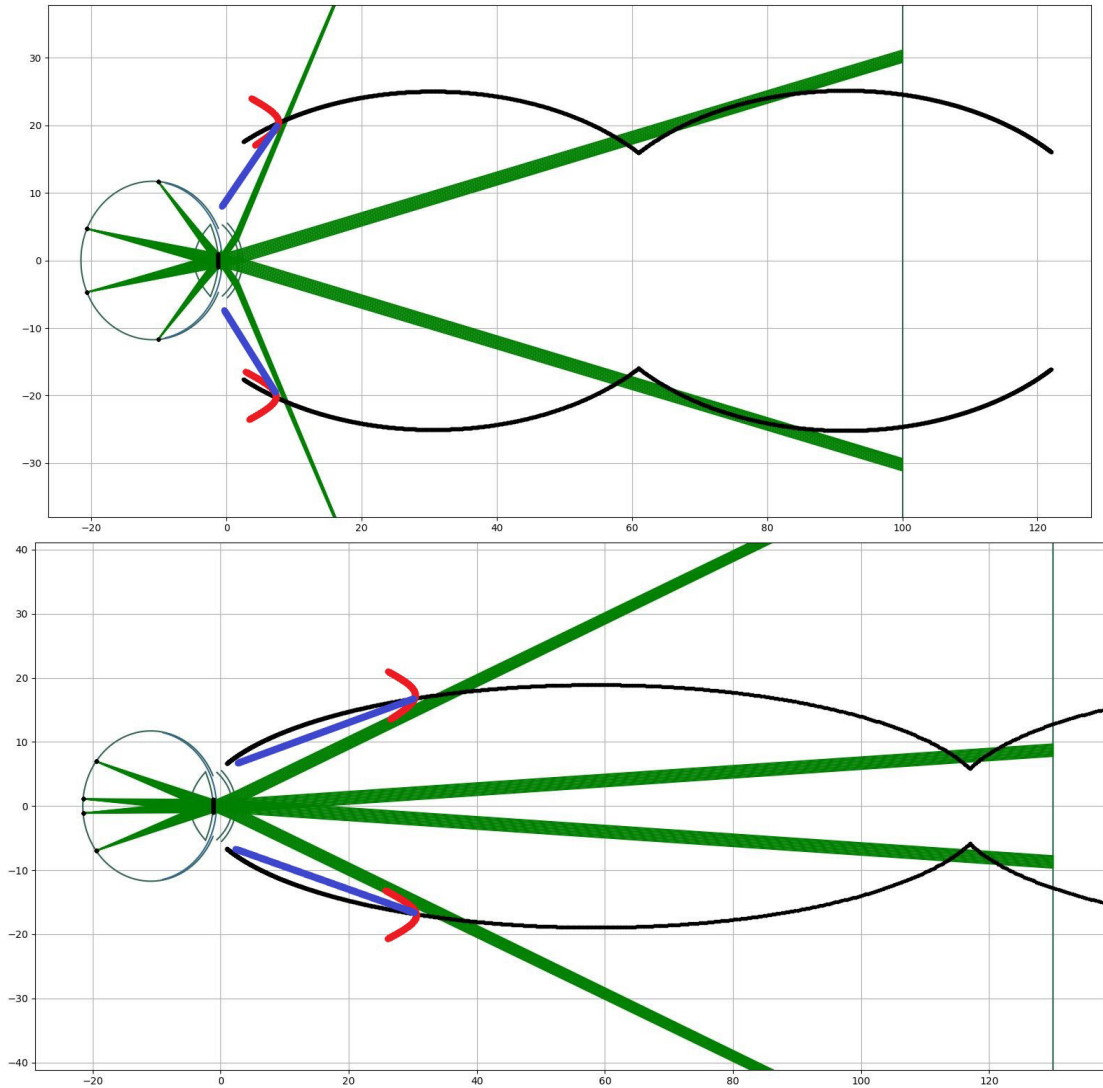

Figure 6.1: Image showing the regions to be cut for aplanats from first and second phase. The regions before the red curves can be cut and a masking can be put along the blue straight line.

6.2.2 Processing the constructed 3D image of retina

The reconstructed 3D images have blurring to a little extent near the peripheral regions due to the contributions from neighboring points on retina in a patch and aberrations due to eye lens. The degree of contributions from those neighboring points can be viewed after constructing the weight matrix as described in this thesis. A signal processing technique has to be developed by studying the non-linear properties of the system and correcting transformation or filters need to be designed.

6.2.3 New illumination method

In all the simulations, an assumption has been made that retina is uniformly illuminated and that light is reflected by it uniformly. The process of injecting light into the eye and uniformly illuminating the retina for the system proposed needs to be designed.

One method that can be used is to build aplanats with materials which act like one-way mirrors, allowing external light to enter but blocking the light coming from eye to leave the aplanat.

6.2.4 Varying human eye models

In this thesis, all the simulations were performed on a standard model of eye in a relaxed state and the sensors designed depend upon the shape of the eye and the power of that eye-lens. So the future work should also incorporate factors like different shapes of eye-balls and different powers of eye-lens.

A small observation that was made is that, as the size of retina increases, the sensor shape widens and vice versa. Also with increase in bulging of the eye-lens, the sensor shape will again widen.

References

[1] [Online]. Available: https://www.indiatoday.in/education-today/gk-current-affairs/story/world-sight-day-2017-facts-and-figures-1063009-2017-10-12

[2] [Online]. Available: https://en.wikipedia.org/wiki/Fundus_photography

[3] [Online]. Available: https://www.opsweb.org/page/fundusphotography

[4] [Online]. Available: https://en.wikipedia.org/wiki/Spherical_aberration

[5] [Online]. Available: https://en.wikipedia.org/wiki/Coma_(optics)

[6] [Online]. Available: https://en.wikipedia.org/wiki/Chromatic_aberration

[7] Donaldson, David D., Rochelle Prescott, and Stephen Kennedy. "Simultaneous stereoscopic fundus camera incorporating a single optical axis." Investigative ophthalmology & visual science 19.3 (1980): 289-297.

[8] Gross, Herbert, Fritz Blechinger, and Bertram Achtner. Human eye. WileyVCH Verlag GmbH & Co. KGaA, 2008.

[9] Abrmoff MD, Garvin MK, Sonka M. "Retinal Imaging and Image Analysis." IEEE reviews in biomedical engineering. 2010;3:169-208. doi:10.1109/RBME.2010.2084567.

[10] DeHoog Edward, and James Schwiegerling. "Fundus camera systems: a comparative analysis." Applied optics 48.2 (2009): 221-228.

[11] N. Shibata and M. Torii, "Fundus camera, U.S. patent 6,654,553 (25 November 2003)

[12] Panwar, N., Huang, P., Lee, J., Keane, P. A., Chuan, T. S., Richhariya, A., , Teoh, S., Lim, T.H. and Agrawal, R. (2016). "Fundus photography in the 21st centurya review of recent technological advances and their implications for worldwide healthcare." Telemedicine and e-Health, 22(3), 198-208.

[13] Delori, F. C., Webb, R. H. & Sliney, D. H. Maximum permissible exposures for ocular safety (ANSI 2000), with emphasis on ophthalmic devices. J. Opt. Soc. Am. A 24, 12501265 (2007).

[14] DeHoog, E., and J. Schwiegerling. "Optimal parameters for retinal illumination and imaging in fundus cameras." Applied optics 47.36 (2008): 6769-6777.

[15] Head, A. K. "The two-mirror aplanat." Proceedings of the Physical Society London. Section B 70.10, 945-949(1957).

[16] Nakar, Doron, Daniel Feuermann, and Jeffrey M. Gordon. "Aplanatic near-field optics for efficient light transfer." Optical Engineering 45.3 (2006): 030502.

[17] Feuermann, Daniel, and Jeffrey M. Gordon. "High-irradiance reactors with unfolded aplanatic optics." Applied optics 47.31 (2008): 5722-5727.

[18] Escudero-Sanz, Isabel, and Rafael Navarro. "Off-axis aberrations of a wide-angle schematic eye model." JOSA A 16.8 (1999): 1881-1891.

[19] Dubbelman, Michiel, and G. L. Van der Heijde. "The shape of the aging human lens: curvature, equivalent refractive index and the lens paradox." Vision research 41.14 (2001): 1867-1877.

[20] Von Noorden, Gunter K. "Binocular vision and ocular motility." Theory and management of strabismus 70 (1996): 111370-372406.

[21] Atchison, David A., et al. "Shape of the retinal surface in emmetropia and myopia." Investigative ophthalmology & visual science 46.8 (2005): 2698-2707.

[22] Hermans, Erik A., et al. "Constant volume of the human lens and decrease in surface area of the capsular bag during accommodation: an MRI and Scheimpflug study." Investigative ophthalmology & visual science 50.1 (2009): 281-289.